Proceedings of the Institution of Mechanical Engineers, Part P: Journal of Sports Engineering and Technology

https://doi.org/10.1177/1754337119831107

Article Information

Article first published online: April 2, 2019

Received: February 14, 2018; Accepted: January 17, 2019

Email: n.ladommatos@ucl.ac.uk

Influence of air rifle pellet geometry on aerodynamic drag
Nicos Ladommatos

Department of Mechanical Engineering, University College London (UCL)

Abstract

Air rifles and air pistols find widespread use in formal and recreational sports events. Despite their widespread use in sport, they have rarely been studied scientifically. The influence of air rifle pellet geometry on aerodynamic drag was investigated experimentally and theoretically at Mach number of 0.58 (approximately 200 m/s) and Reynolds number of 54,000 using a low-turbulence open wind tunnel. Measurements were made of surface pressure and aerodynamic drag distribution for five pellets having different geometries. Pellet overall drag was also measured with a load cell system. Theoretical analysis based on 2-D potential flow theory was used to study the relationship between nose shape and drag.

Results indicate that the overall drag of non-spherical pellets was dominated by the drag on their front face, with the face contributing approximately 65 % of the overall pellet drag, while base drag contributed almost all of the remaining 35 %. The *net drag contribution* of the pellet side-slopes was close to zero. The geometry of the front face had a weak influence on the drag acting on the pellet base. This influence was exercised through the behaviour of the free shear layer separating from the pellet head rim. It was apparent that the presence of the tail in a dome-head pellet enabled flow reattachment and a rise in base pressure, which reduced the base drag. In contrast, at Re ~ 54,000, flow reattachment on the rear surface of the spherical pellet was not possible. For this reason, its base drag was higher than that for the dome-head pellet. Flat-, cone-, and cavity-head pellets had higher *overall drag coefficient*

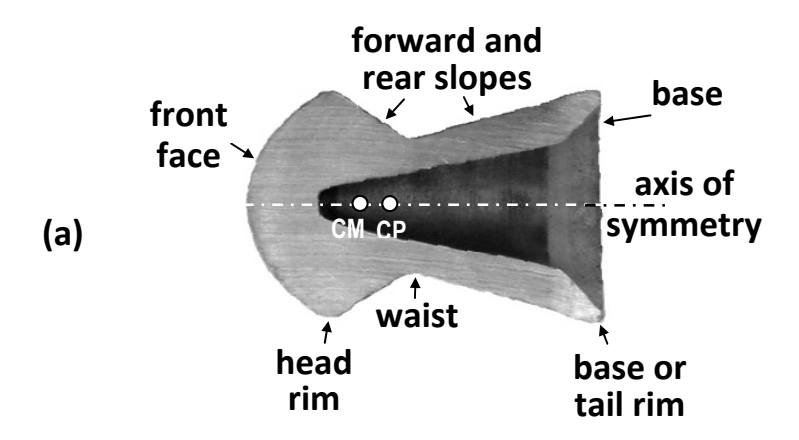
1

values than a spherical pellet. The higher overall coefficients were due to the higher face drag than the spherical pellet, which was not compensated sufficiently by their lower base drag.

1 Introduction

Major international and national sports competitions (Olympic Games, European and World Championships) include air rifle and air pistol events. Air rifle and pistol target practice is also a popular recreational sport worldwide and in the UK alone, up to five million individuals participate. [1] Aerodynamic drag is a major influence on air rifle pellet trajectory and shot accuracy. Once the pellet leaves the rifle barrel and assumes free flight, aerodynamic drag opposes the motion of the pellet, slowing it down. This prolongs the pellet flight period, during which time gravity and aerodynamic forces acting on the pellet cause it to deviate in a complex manner from a linear path to the target. Despite the key role of aerodynamic drag on pellet trajectory, few scientific studies have been published on this topic. [2] [3] [4] This contrasts with a plethora of aerodynamic studies for balls and other projectiles in sports such as golf, [5] badminton, [6] football/soccer, [7] [8] baseball, [9] tennis, [10] table tennis, [11] [12] cricket, [13] and frisbee. [14] Aerodynamic drag of ordnance projectiles has been extensively researched for many decades, however, little data has been published in scientific literature.

This paper explores the relationship between aerodynamic drag and air rifle pellet geometry for several commercially available pellets of 4.5 mm (0.177 in) calibre. The great majority of commercially available pellets are manufactured from soft pure or alloyed lead, while a few are made from harder metals such as tin, or partially from polymers or steel. Pellets come in a wide variety of shapes, which range from that of a sphere to the common diabolo shape shown in Fig. 1.



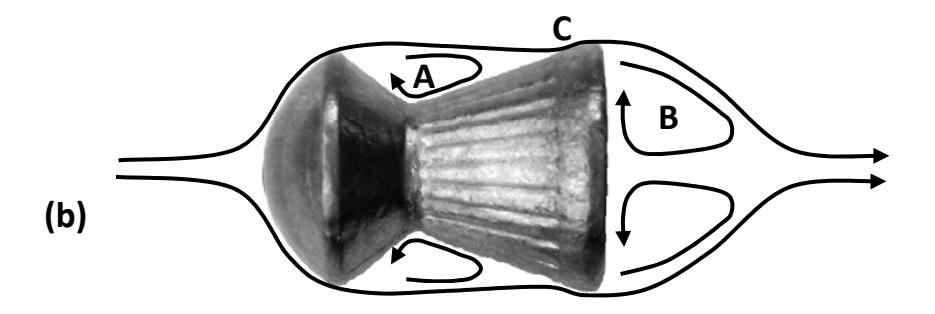


Figure 1 Geometry and flow around a pellet (a) Pellet cross section and geometry (CM is the pellet centre of mass and CP is the centre of pressure) (b) Main flow regions

The value of drag coefficient (C_d) for commercial 4.5 mm calibre pellets varies widely, depending on pellet geometry and Mach number (M_a). For example, at $M_a \sim 0.6$ the C_d value varies between 0.3 and 0.8. By comparison, the C_d value for firearm bullets is generally smaller. At transonic speeds of $M_a \sim 0.8$ to 0.95, the C_d value for 5.56, 5.59 and 7.62 mm calibre bullets ranges from about 0.2 to 0.3. [15] [16] [17] Lastly, the C_d value for 4.5 mm smooth spheres at $M_a \sim 0.6$ is approximately 0.50. [18] [19]

Air rifle and pistol pellets fly through the atmosphere usually at subsonic speeds, which range from Mach number of approximately 0.5 to 0.8. During pellet free flight, flow separation often occurs at the head rim as shown in Fig. 1, with the flow often re-attaching close to the pellet tail rim near point C, but only to detach once again at the tail rim. The detaching boundary layers at the head and tail rims form free shear layers which engulf low pressure recirculation zones labelled A and B in Fig. 1(b). Separation of the flow from the pellet head and tail rims is an important contributory factor to pellet drag, as it causes lower pressures within the separation regions A and B, which contribute substantially to pellet drag. For example, the low pressure recirculation region B, downstream of the pellet base, contributes a significant proportion of the total pellet drag (at least 35 % at $M_a \sim 0.6$, see later). The pellet shown in Fig. 1 has a fairly rounded front face so that the flow separating close to the head rim does so at an angle of approximately 45° to the pellet axis. In the case of pellets with a blunt flat face, the separating flow will leave the pellet rim at a greater angle of up to 90° , resulting in wider separation zones and wake and generally higher pellet drag.

Pellets almost invariably have a hollow blunt base, and when they are in free flight, their large base area is exposed to the low pressure recirculation region B (Fig. 1). The design of

the hollow base is deliberate. When the pellet is inside the rifle barrel, propelled by high pressure gas, the gas pressure expands the base rim and forces it into the barrel rifling grooves, so as to seal the propelling gases. The barrel helical grooves force the pellet to spin, so that it leaves the barrel gyroscopically stabilised, similar to firearm bullets. The deep hollowing of the pellet shown in Fig. 1(a) moves the pellet centre of mass (CM) forward so that it lies *ahead* of the centre of pressure (CP). This provides aerodynamic stabilisation, so that when the pellet leaves the barrel and assumes free flight, it is stabilised aerodynamically and gyroscopically.

In contrast to air rifle pellets, which have blunt tails, firearm bullets generally have gradually tapered "boat" tails, with the tail diameter gradually reducing toward their tail end to avoid separation of the flow from the side surfaces of the bullet tail. The tail tapering decreases the base area of the bullet that is exposed to the low pressure recirculation region downstream of the base, thus reducing the base drag. The tapered tail also encourages pressure recovery along the sides of the tail, which raises the base pressure and reduces drag further. [20] [21] [22] Mair [20] studied the reductions that could be obtained by adding boat tails to truncated blunt-base projectiles. Reductions of more than 50 % in base drag were obtained by adding to the blunt base a short (~ 0.5 calibre long) boat tail afterbody having gradual downstream taper of 22°.

2 Experimental approach and systems

2.1 Pellets investigated

Figure 2 shows the five pellets investigated, all of which had 4.5 mm head diameters (0.177 calibre). All of the pellets were made of lead and are currently available commercially. The first pellet was spherical, the second had a domed-faced head, the third had a flat-faced head with a head rim chamfer, and the fourth had a cone-faced head. The fifth pellet had a truncated cone face, with the apex replaced by a deep cavity, but was otherwise almost identical to the fourth pellet with the cone-shaped head.

For the measurement of drag coefficient, all pellets were mounted on identical stings, as shown in the lower part of Fig. 2. The stings were made of ground high-carbon steel rod of 1 mm diameter, attached securely inside the pellet base cavity using epoxy adhesive. During the curing of the adhesive, a custom-made jig ensured that the sting and pellet axes were

aligned accurately. The sting cross sectional area was 4.94 % of the pellet cross sectional area at its head rim. Norman and McKeon [23] used particle image velocimetry to investigate the effect on sphere wake of sting/sphere sectional area ratio. They found that ratios below 6.25 % had no significant influence on the wake. Hoerner [24] also conducted tests with spheres during which the rear-mounted sting diameter was increased from an area ratio of 0.64 % to 4 % and found no significant difference in the drag coefficient at subcritical values of Reynolds number.

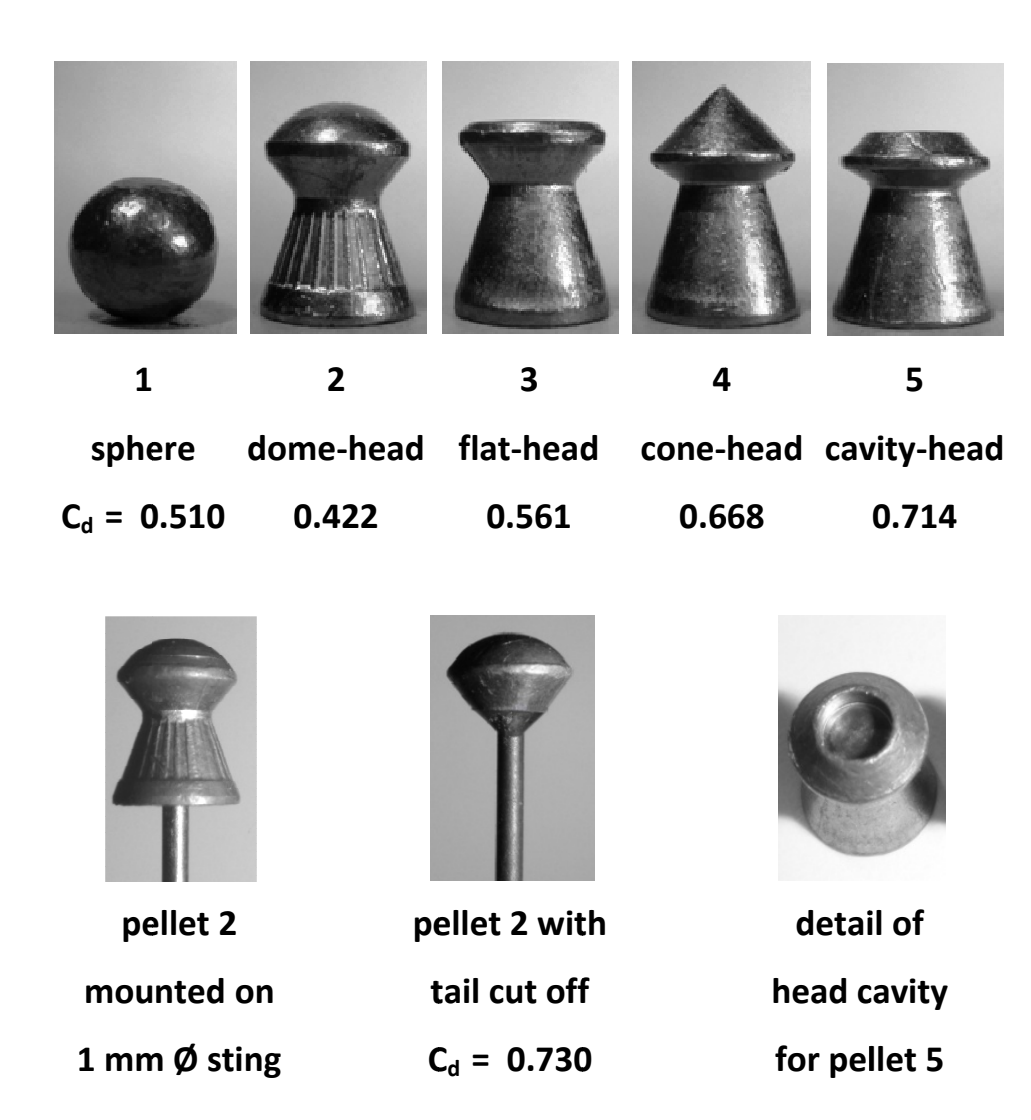
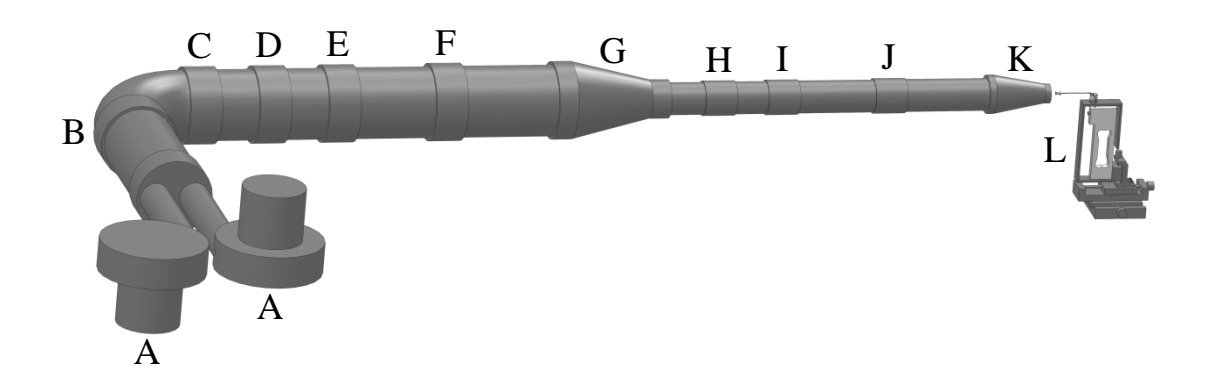


Figure 2 The five pellets investigated and their values of drag coefficient measured with a load cell system at Re \sim 54,000 and $M_a \sim$ 0.58. All pellets had head-rim diameters of 4.5 mm

2.2 Open jet wind tunnel

An open jet wind tunnel and associated drag force measuring system were constructed for these investigations and are shown in Fig. 3. Two electrically driven, high-speed, two-stage, centrifugal compressors discharged pressurised air into a 110 mm diameter pipe in which a series of honeycomb and mesh screens reduced swirl and velocity mal-distributions, with very small pressure drop penalty due to the large pipe diameter.

The air flow then passed through a contraction into a 50 mm diameter pipe, where an additional set of honeycomb and mesh screens conditioned the flow and further reduced turbulence intensity. Finally, the air flow passed through a second contraction and emerged through a 17 mm diameter nozzle as a free jet. Both contractions had a curved internal profile (5th order polynomial) so as to minimise the risk of internal flow separation. [25] The jet velocity was controlled by varying the speed of the electrically driven air compressors. The maximum Mach number (M_a) of the free jet available from the tunnel was just under 0.6, corresponding to free stream velocity of approximately 200 m/s.



(A) Two-stage high-speed centrifugal compressors; (B) Settling pipe (110 mm Ø x 720 mm length); (C) Coarse wire mesh (0.8 mm wire Ø, 2.83 mm open width); (D) Hexagonal honeycomb (3.175 mm cell width, 20 mm cell length); (E) and (F) Medium wire mesh (0.355 mm wire Ø, 1.23 mm open width); (G) Contraction 110 mm Ø to 50 mm Ø, 1.21 ratio length/inlet diameter, 5th order polynomial internal profile; (H) Hexagonal honeycomb (3.175 mm cell width, 20 mm cell length); (I) Medium wire mesh (0.355 mm wire Ø, 1.23 mm open width); (J) Fine wire mesh (0.22 mm wire Ø, 0.94 mm open width); (K) Contraction 50 mm Ø to 17 mm Ø, 1.26 ratio length/inlet diameter, 5th order polynomial internal profile; (L) Pellet drag force measuring system

Figure 3 Open wind tunnel system

2.2.1 Air jet velocity distribution

Calculation of the free jet velocity (U) took compressibility effects into account due to the fairly high Mach number at which the pellet drag measurements were made ($M_a \sim 0.6$). The calculation relied on measurements of the free jet stream stagnation and static pressures (p_o , p) made with a small pitot tube (0.8 mm i.d.). First, the free stream Mach number, M_a , was calculated for isentropic flow from the following expression as shown in Eq. (1):

$$\frac{p_o}{p} = \left(1 + \frac{\gamma - 1}{2} M_a^2\right)^{\frac{\gamma}{\gamma - 1}} \tag{1}$$

Using the value of M_a evaluated from Eq. (1), the jet dynamic velocity head was then calculated from the following expression in Eq. (2) and used later for calculation of the pressure and drag coefficients,

$$\frac{1}{2} \rho U^2 = \frac{1}{2} \gamma M_a^2 p \tag{2}$$

where ρ is the jet free stream density. In subsequent discussions in this paper, the value of the free jet velocity, U, was quoted and this was calculated from the following expression shown in Eq. (3):

$$U = M_a \sqrt{\gamma R T} \tag{3}$$

The free jet static temperature, T, was calculated for isentropic flow using the measured stagnation pressure and stagnation temperature (p_{oo} , T_{oo}) in the wind tunnel, just upstream of the jet nozzle contraction as shown in Eq. (4):

$$T = T_{oo} \left(\frac{p}{p_{oo}}\right)^{\frac{\gamma - 1}{\gamma}} \tag{4}$$

Figure 4 shows the radial profile of the free jet velocity measured at 0, 10 and 20 mm downstream of the nozzle exit plane. At 10 mm, the radial velocity profile was flat at \sim 205 m/s up to \pm 8 mm from the jet centreline. Therefore, the \pm 2.25 mm head radii of the 4.5 mm pellets were readily encompassed within this flat profile. All subsequent measurements of drag and pressure distributions were made with the front of the pellet nose placed at 10 mm from the nozzle exit plane.

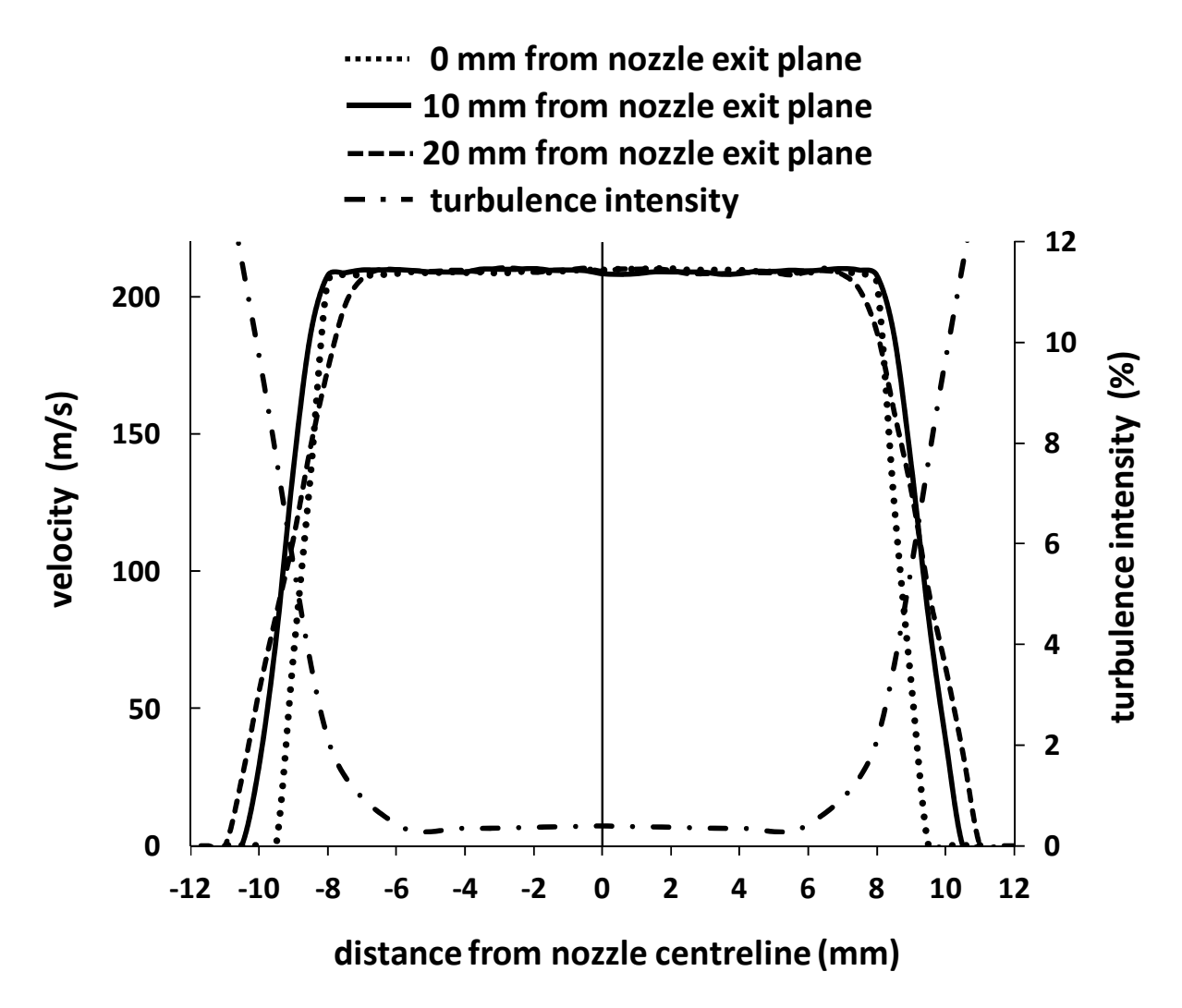


Figure 4 Velocity profiles and turbulence intensity for open wind tunnel air jet at $M_a = 0.58$ and Re = 54,000

Pellet C_d values were measured at approximately 205 m/s ($M_a \sim 0.58$). This velocity corresponds to kinetic energy values between 10 J and 13 J, depending on the mass of the five pellets investigated. For comparison, the legal limit of kinetic energy for air rifles in many countries, including the UK, is just over 16 J.

2.2.2 Blockage ratio

The blockage ratio, defined as the pellet maximum cross sectional area divided by the jet nozzle cross sectional area, was ~ 7.5 % for the 4.5 mm pellets investigated. This value was in the middle of the range of 0.4 to 11 % quoted by various authors who conducted studies of aerodynamic drag for a variety of bodies in open jet wind tunnels. [26] [27] [28] [29] [5] [30] [31] Maskel [32] provides correlations which can be used to correct for blockage effects in

closed wind tunnels, where the presence of a solid model between constraining walls tends to increase the flow velocity around the model. Barlow et al. [33] suggested limiting the blockage ratio below 7.5 % in *closed tunnels*, while they also stated that blockage effects in open jet tunnels are smaller than those in closed tunnels. In open wind tunnels, as the one used here, the unconstrained jet is free to expand radially around the pellet, in a manner similar to that of the unconstrained atmosphere being displaced around a flying pellet.

2.2.3 Turbulence intensity

The turbulence intensity of the free jet was measured using a custom-build hot wire anemometer probe constructed with 5 µm tungsten wire, 1.24 mm long, which was spotwelded at the tips of ~ 0.5 mm stainless steel needle prongs. The wire was operated in constant temperature mode using a custom-build servo-amplifier, constructed along the lines described by Itsweire and Helland [34] and Osorio et al. [35] At 204 m/s, the square wave test response of the probe/amplifier system was high, at 17 kHz (bridge ratio 5, overheat ratio 0.5, and jet temperature compensation was as suggested by Bruun [36] and Benjamin and Roberts [37]).

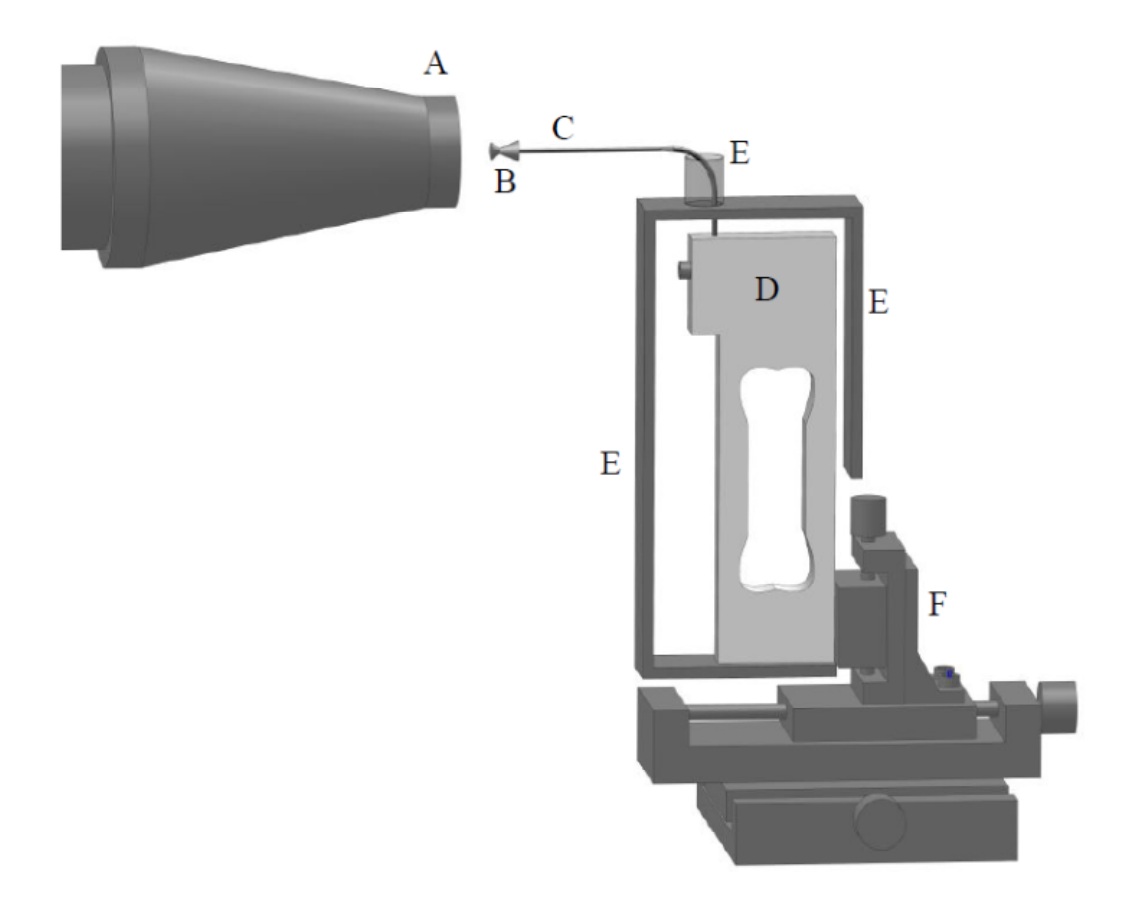
Measurements of turbulence intensity were made radially by traversing across the free jet at a distance of 10 mm downstream of the nozzle exit plane when the jet velocity was at 204 m/s ($M_a \sim 0.58$). Figure 4 shows that the turbulence intensity was 0.35 % at the free jet centreline and it stayed at approximately that level as the jet was traversed radially up to a radius of approximately 6 mm from the jet centreline. The intensity then rose gradually to ~ 2 % as the radius of 8 mm was approached, and then it rose sharply when the radius was increased beyond 8 mm, indicating the presence of a highly turbulent shear layer at the interface of the jet and the stationary atmosphere (the nozzle radius was ± 8.5 mm).

The above values indicate that the turbulence intensity of the open tunnel was low. It compares favourably with values of turbulence intensity ranging from 0.30 to 2.5 % at the centreline of open wind tunnels described in published sources. [5] [38] [31] [28] [29] [30] [39] [40] [41] The low level of free stream turbulence measured at M_a = 0.58 and 10 mm downstream of the nozzle exit plane suggests that turbulence was not a significant influence on the measured values of drag and pressure coefficients presented in this paper.

2.3 Measurement of pellet drag

The pellet drag was measured using the load-cell system shown in Fig. 5. The pellets were positioned with their nose 10 mm downstream of the nozzle exit plane. The pellet support comprised two sections, the pellet sting itself (1 mm o.d. x 20 mm long) followed by a curved sting extension (1.5 mm o.d.) which was attached to a strain-gauged load cell that measured the pellet drag force. The shear load cell, normally used in precision balances of 1 mg resolution, was insensitive to variations in the location of the point of loading and side loads. Part of the sting support and the load cell itself were shielded from the air flow so as to minimise the tare drag force on the pellet. This proved to be crucial in achieving high repeatability of the measured value of C_d. The voltage output from the load cell strain-gauge bridge was amplified and recorded by a 12 bit digital data acquisition system. The output of the combined load cell/amplifier/data acquisition measurement chain was calibrated regularly using known weights (1 mg resolution), with the calibration curve found to be highly linear $(R^2 = 0.9998)$. Analysis of the load cell system hysteresis was carried out using data recorded from loading and unloading the load cell system. The measured hysteresis width of the load cell system was 0.7 % at the average pellet drag force of approximately 25 grams. The load cell was mounted on a 3-D positioning stage, which allowed the pellet axis to be aligned accurately with the nozzle axis, with the aid of an aligning jig.

When the pellet was mounted, the air flow imposed drag forces, not just on the pellet but also on the pellet support sting. Therefore, the force measured by the load cell, was the *gross* drag value, which included the air drag force on the pellet itself plus the "tare" drag due to the air jet impinging on the sting. In order to evaluate the *net* drag on the pellet, the tare drag on the sting was measured (after each measurement of the gross drag), using the additional arrangement shown in Fig. 6. An identical pellet was mounted, using a transverse sting (item D in Fig. 6), to a support system (items E, F, G) which was independent of the load cell. An axial "dummy" sting (item C), *not connected* to the pellet, was placed in position and attached to the load cell of Fig. 5. Thus, the arrangement of Fig. 6 allowed the tare drag on the dummy axial sting to be measured and subtracted from



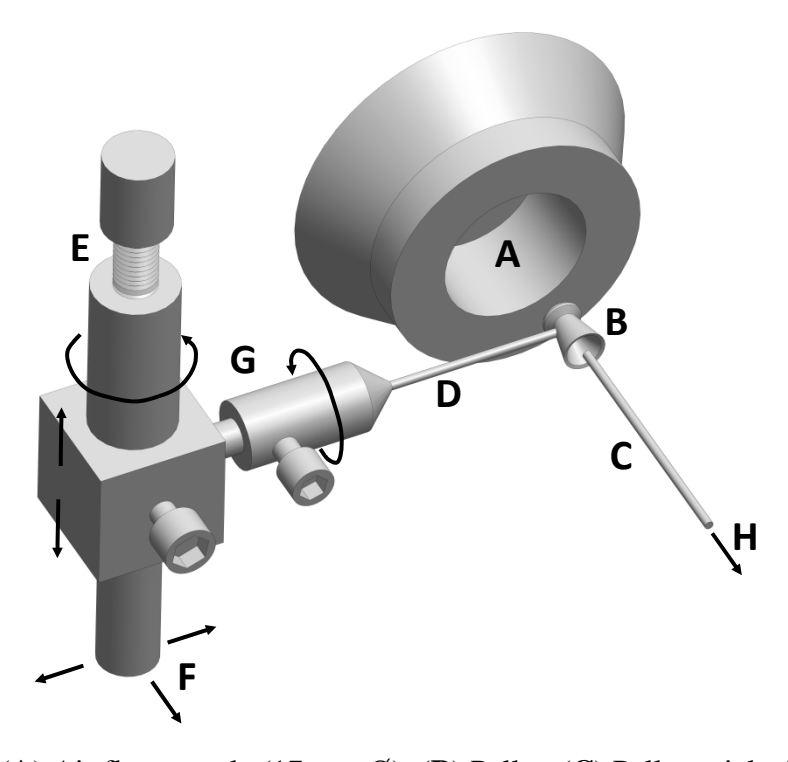
(A) 17 mm Ø nozzle; (B) Pellet; (C) Pellet sting (1 mm Ø x 20 mm long + 1.5 mm Ø curved support); (D) Shear-force load cell; (E) Air shield for load cell and sting (no contact with sting, except at bottom of load cell; side shields not shown for clarity); (F) Three dimensional traverse (X, Y, Z)

Figure 5 Pellet drag force measuring system

the overall (gross) drag, resulting in the required value of *net* drag force acting on just the pellet. This pellet overall *net* drag force was then used to calculate the pellet drag coefficient as shown in Eq. (5):

$$C_d = \frac{drag\ force}{\frac{1}{2}\rho U^2\ A} \tag{5}$$

where drag force is the *net* drag force and A is the pellet cross sectional area at the pellet head rim.



(A) Air flow nozzle (17 mm Ø); (B) Pellet; (C) Pellet axial sting
(1 mm Ø) (not attached to pellet); (D) Pellet transverse sting (1 mm Ø);
(E) Pellet elevation adjusting mechanism; (F) Pellet two-dimensional translation system (mechanism not shown); (G) Pellet rotation mechanisms; (H) Axial sting attached to load cell for measuring tare drag force on axial sting (see Fig. 5 for attachment details)

Figure 6 Arrangement for measuring tare drag on the axial sting

2.4 Measurement of pressure distribution around the pellets

The pressure distribution on the surface of the four pellets numbered 2 to 5 in Fig. 2 was measured as illustrated in Fig. 7. A hole of 0.2 mm diameter (item A) was drilled on the pellet surface so that the hole formed a pressure tapping that communicated with the internal cavity of the pellet. The pellet was then secured onto a flanged stainless steel tube (item B in Fig. 7) and sealed using instant adhesive. The tube was then used as a sting to support the pellet with its nose at 10 mm downstream of the wind tunnel nozzle exit. The other end of the tube was connected to a pressure transducer using flexible small-bore tubing. In this way, pressure was measured at 18 tapping locations around the pellet, numbered 1 to 18 in Fig. 7. A new identical pellet was used for each new tapping hole location, with all 18 pellets purchased in a single batch. This set of 18 surface pressure measurements was supplemented

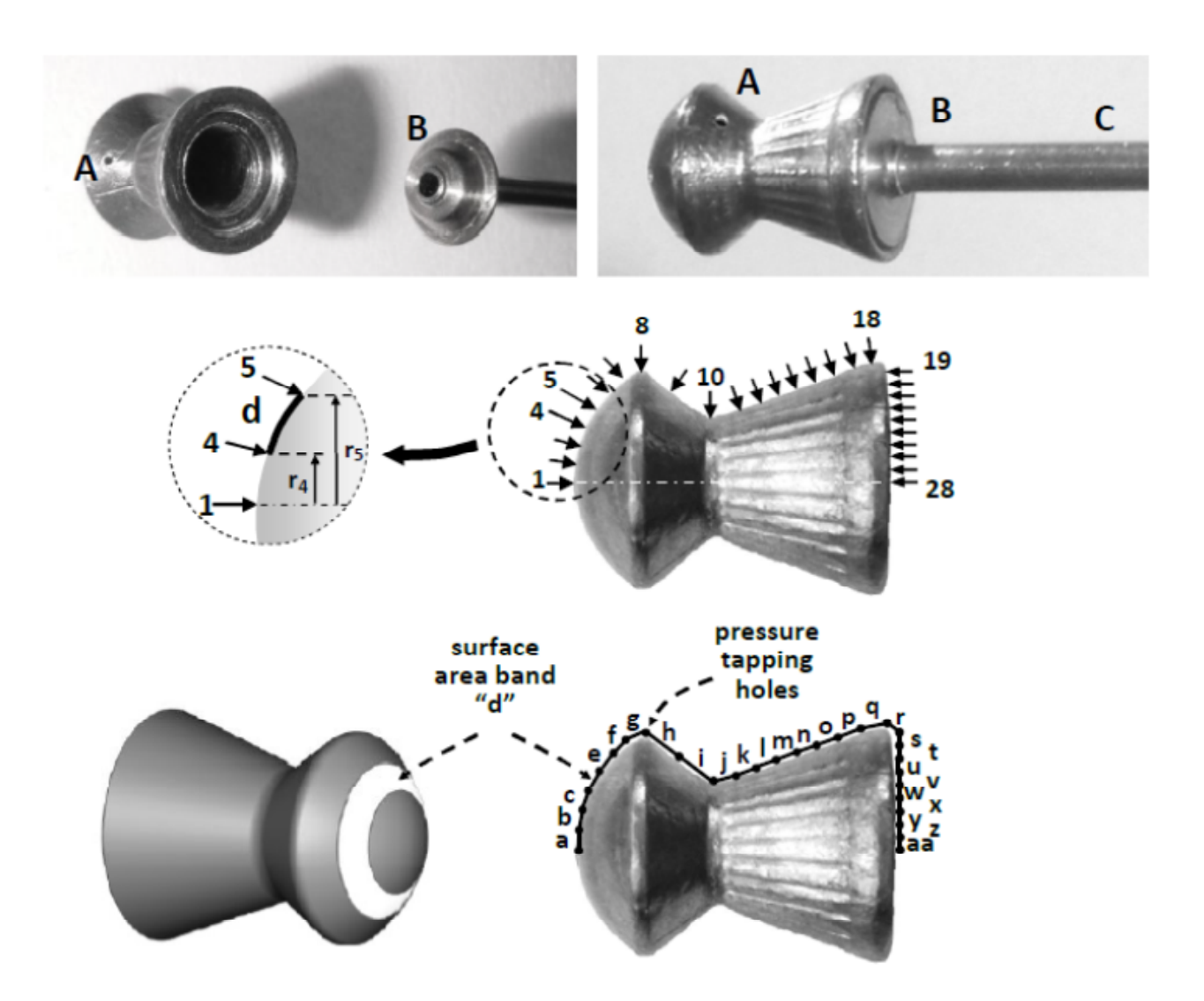
by an additional set of 10 measurements of pellet base pressure, made at radial locations numbered 19 to 28 in Fig. 7. These 10 measurements of base pressure distribution were made with a micro-pitot tube (0.45 mm $\,$ i.d., 0.80 mm o.d.) positioned ~ 0.2 mm downstream of the pellet base plane on a radial traverse system.

The 28 surface pressure measurements around the pellet were also used to analyse the drag distribution around the pellet by means of pressure-area numerical integration. The surface of the pellet and its base were divided into a number of surface area "bands" as shown in Fig. 7. The area bands are labelled with letters "a", "b", "c", etc. in order to distinguish them from the pressure tapping locations labelled with numbers 1, 2, 3, etc. Each surface area band lay between two pressure tapping holes or two base pressure measurements in the case of the pellet base. As an example, the inset schematic in Fig. 7 shows that the area band labelled "d" (on the front face of the pellet) lay between the two pressure tappings 4 and 5. The pressure, p_d, that acted on the surface of area band "d", was considered to be the average of the pressures measured at tappings 4 and 5, that is, $p_d = \frac{p_4 + p_5}{2}$. The pressure force that acted in the normal direction to surface area band "d" was $F_d = (p_d - p_a)A_d$, where A_d was the area of pellet surface band "d". The force, F_d , for band "d" was then resolved in the pellet axial direction in order to calculate the contribution of band "d" to the overall pellet drag. Denoting the resolution of force, F_d , in the axial direction as, F_{dx} , this resolved force was calculated, most conveniently, using the resolved area of band "d" in the axial direction, that is $\pi (r_5^2 - r_4^2)$ (see Fig. 7). Therefore, as shown in Eq. (6) F_{dx} is

$$F_{dx} = \left(\frac{p_4 + p_5}{2} - p_a\right) \pi (r_5^2 - r_4^2)$$
 (6)

The calculated axial drag force F_{dx} from band "d" was a result of the mean pressure of band "d", $p_d = \frac{p_4 + p_5}{2}$, deviating from the atmospheric pressure p_a .

The axial force contributions of all 27 area bands around the pellet were then summed algebraically, which provided the overall pellet net drag force, F_D. This overall net force was then entered as the drag force in Eq. (5) in order to calculate the pellet overall drag coefficient.



(A) 0.2 mm diameter tapping hole; (B) Pellet tail flange; (C) Support sting/pressure tube 1.25 mm o.d. The locations of some of the pressure tapping holes were as follows: Tapping 1 was on pellet axis; 4 was offset radially by r_4 = 0.96 mm from pellet axis; 5 was offset radially by r_5 = 1.29 mm; 8 was on the pellet head rim and offset 2.25 mm from pellet axis, etc.; pressure measurements for pellet base at locations 19 to 28 were made with a micro-pitot tube (0.45 mm i.d. 0.80 mm o.d.)

Figure 7 Arrangements for measurement of pressure distribution around 4.5 mm calibre pellets (numbers 1, 2, 3, etc, are the locations of pressure tapping holes; letters a, b, c, etc., are the area "bands" *between* pairs of tapping holes)

In this paper, values of pressure coefficient were evaluated using the following general expression for pressure coefficient as shown in Eq. (7),

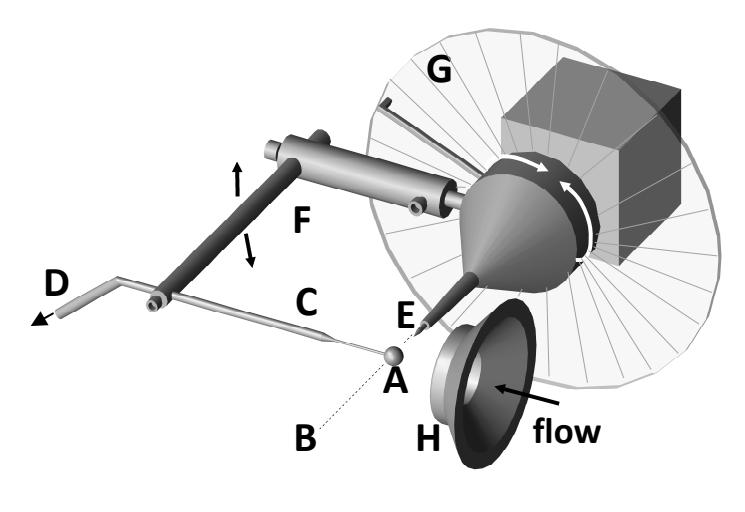
$$C_p = \frac{p_s - p}{\frac{1}{2}\rho U^2} \tag{7}$$

where C_p is the pressure coefficient, p_s , is a pressure on the surface of a pellet, and p is the *free stream static pressure* measured with the pitot tube (invariably, the measured free stream static pressure was found to be equal to the atmospheric pressure, p_a , as the stream was a free jet).

In the case of pellets numbered 2, 3, 4 and 5, the pressure coefficient was calculated for each surface area band. For each surface area band, the value for p_s that was used in Eq. (7) was the average pressure for that area band (for example, in the case of surface band "d", pressure $p_s = p_d = \frac{p_4 + p_5}{2}$, where p_4 and p_5 were the pressures measured at pressure tappings 4 and 5, on either side of band "d").

A somewhat different experimental arrangement was used to obtain the pressure distribution around the 4.5 mm spherical lead pellet (numbered 1 in Fig. 2). This arrangement took advantage of the perfect symmetry of the spherical pellet and it involved only a single spherical pellet with a single pressure tapping hole. As shown in Fig. 8, a 0.2 mm diameter pressure tapping hole was drilled on the surface of the spherical pellet. The hole was arranged so that it communicated via a stainless tubular sting and flexible rubber tubing with a pressure transducer. The pellet could be rotated, by means of a supporting frame, about a *fixed transverse axis* which passed through the centre of the spherical pellet.

The tapping hole could be positioned at any azimuthal angle θ^{o} on a 180° semi-circular arc, which extended from the stagnation point, on the front face of the pellet when facing the flow, to a diametrically opposite point at the centre of the pellet rear face, as shown in more detail in Fig. 9.





(A) Spherical pellet (size exaggerated for clarity); (B) fixed axis of rotation through pellet centre; (C) stainless steel two-part tubular sting (0.8 mm and 2 mm o.d. tubes); (D) flexible rubber tube to pressure transducer; (E) sliding point for checking pellet rotation axis; (F) frame for rotation of pellet about fixed axis B; (G) stationary protractor for setting pellet rotation angle; (H) flow nozzle; (I) 0.2 mm pressure tapping hole on spherical pellet surface

Figure 8 Arrangement for measuring the pressure distribution around the 4.5 mm diameter spherical lead pellet

The pressure measurements at each taping azimuthal angle, θ° , were used to calculate the surface pressure coefficient at each angle, θ° , using Eq. (7) above. In the case of this pellet, the value of p_s in Eq. (7) was the pressure measured at the tapping hole when the hole was located at azimuthal angles, θ° , between 0° and 180° . The pressure coefficient calculated at each azimuthal angle is plotted in Fig. 9 against angle θ° . Numerical integration of the pressure coefficient curve shown in Fig. 9 over 2 x 180° provided an estimate of the value of the overall drag coefficient for the spherical lead pellet, as shown in Eq. (8):

$$C_d = 2\sum_{\theta=0}^{\pi} C_p \sin\theta \cos\theta \ \Delta\theta \tag{8}$$

where $\Delta\theta$ was the increment in azimuthal angle θ between successive pressure measurements. An implicit assumption was that the pressure measured at the tapping was uniform around the pellet circumference in the plane normal to the flow. This assumption was considered to be reasonable because the velocity profile across the free stream jet was found to be uniform and also because care was taken to ensure that the pellet axis of rotation was accurately positioned perpendicularly to the flow. The estimate of pellet overall C_d obtained from Eq. (8) using the pressure distribution was then compared with the value of pellet overall C_d obtained independently using the load cell arrangements in Figs. 5 and 6.

2.5 Uncertainty analysis

2.5.1 Repeatability of C_d measured with load cell

The load cell system shown in Figs. 5 and 6 was used to make measurements of the value of C_d for the five pellets shown in Fig. 2. Measurements of C_d for each pellet were made at least three times on different days, providing an indication of the repeatability of C_d measurement. In total, 18 repeat measurements of C_d were made for the five pellets. The *maximum* % *deviation* from a pellet mean value was calculated to be 4.2 % and the minimum was 0.04 %. The *standard deviation* of the 18 values for % *deviation* was 1.3 %. These results therefore provided an estimate of 1.3 % for the repeatability of any individual C_d measurement (standard deviation from the mean).

2.5.2 Accuracy of C_d measurements with load cell system

Error propagation analysis [42] was carried out in order to estimate the accuracy of the value of C_d measured with the load cell system. Uncertainties in the measurements of individual derived variables were estimated to be: drag force, 2.9 %; pellet head cross sectional area, 0.3 %; density, 2.3 %; velocity squared, 2.1 %. Therefore, the *overall error* in the measurement of the pellet C_d was estimated at 4.2 %.

The following factors were found to be crucial in achieving high repeatability and accuracy of C_d measurements: precise alignment of the pellet axis of symmetry with the axis of the jet; minimising pellet tare drag force, by shielding the load cell and pellet sting from the air jet; checking daily the calibrations of the data acquisition and load cell measuring systems; measurement of local atmospheric pressure hourly, using a calibrated pressure transducer.

2.5.3 Accuracy of C_d calculated from surface pressure distributions

Error propagation analysis was also used to estimate the error in overall pellet C_d obtained from surface pressure distribution measurements. The measurement of the radial location of each of the 28 pressure tappings was subject to an estimated random error of 0.05 mm. As can be deduced from Fig. 7, an error in the radial location of a shared tapping almost always

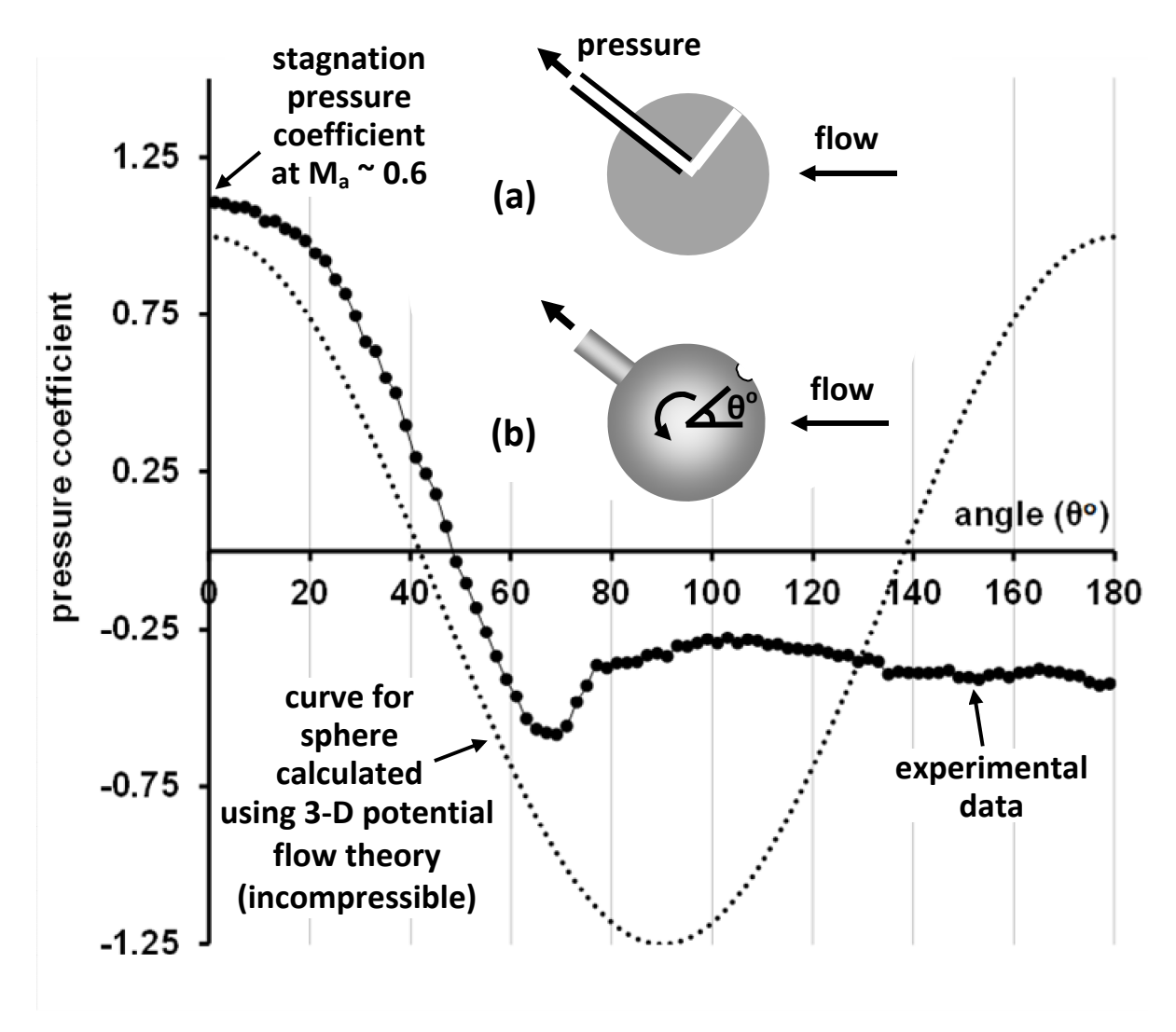


Figure 9 Distribution of pressure coefficient around a 4.5 mm diameter spherical lead pellet at $M_a \sim 0.59$ and Re $\sim 55{,}000$. The inset figures show: (a) cross section of pellet, (b) measurement of surface pressure at various angles θ^o by rotating the pellet

changed the estimated relative area sizes of adjacent bands, but it did not change significantly the calculated overall projected area of the pellet. Rather, such an error introduced a random distortion of estimated drag force distribution around the pellet and an associated error in C_d . This error is not straightforward to estimate, but it is believed that its contribution to the overall error in C_d was small and was thus neglected.

The propagation analysis gave an error estimate of 12.2 % in the value of C_d obtained from surface pressure distribution for each of the four pellets numbered 2 to 5 in Fig. 2. The measurement of pressure at each tapping had an uncertainly of 2.2 % and when this was accumulated over 28 tappings, it accounted for almost all of the overall error of 12.2 % in the value of C_d . The rest of the error resulted from uncertainties in the measurement of pellet head cross sectional area, jet velocity, and jet density.

3 Results

This section presents mostly experimental results of pressure distributions around several pellets and drag coefficients for these pellets obtained using two independent approaches, the load cell system and pressure-area integration. The section also includes results of potential flow analysis in sub-section 3.3, which help in the interpretation of experimental results, in particular how the pellet nose shape affects pressure distribution on the front face of pellets. Because potential flow analysis cannot predict flow separation, this aspect is addressed mainly by the experimental results.

3.1 Pressure distribution and drag for spherical pellet and systems validation

The majority of C_d values presented in this paper were obtained using the load cell arrangements shown in Figs. 5 and 6. In order to assess the accuracy of the C_d values, the load cell system was used to measure the values of C_d for nine small spheres (diameters 3.08 to 4.75 mm), which were then compared with values of C_d for spheres found in published sources. The results are shown in Table 1, which also provides additional information about the small spheres.

The value of C_d was measured at a constant value of $M_a = 0.58$ for all the spheres, while the value of Re for each sphere varied depending on the sphere diameter. For the smallest sphere of 3.08 mm diameter, the Re value was 37,500, while the Re for the largest sphere of 4.75 mm diameter was 57,000.

Table 1 Comparison of measured drag coefficient values for nine small spheres with values of C_d for spheres in published sources

Source of data	M _a	Re	C_d	Difference (C _d - 0.500)
This work (nine spheres) (a)	0.58	37,500 – 57,000	0.49 – 0.51	0 %
Published, Hoerner [18]	0.60	< critical Re value	0.518	+ 3.6 %
Published, Bailey & Hiatt [19]	0.59	50,230	0.51	+ 2.0 %
Published, Jourdan et al. [43] (b)	0.47 to 0.61	37,500 – 48,000	0.54	+8.0 %
Published, Jourdan et al. [43] (c)	0.49 to 0.60	54,500 – 68,500	0.48	-4.0 %

Notes: (a) C_d values were measured for the following nine spheres: six polished hematite spheres with diameters of 3.08, 3.60, 4.02, 4.25, 4.37, 4.50 mm; two stainless steel polished spheres with diameters 4.00, 4.75 mm; one lead spherical pellet with diameter 4.5 mm; (b) accelerating sphere 1.96 mm diameter; (c) accelerating sphere 2.9 mm diameter;

Table 1 shows that the measured values of C_d for the nine spheres ranged from 0.49 to 0.51. This range agrees within 3.6 % of the published value by Hoerner [18] of 0.518 at M_a = 0.60, and within 2 % of the value of 0.51 at M_a = 0.59 given by Bailey and Hiatt [19]. This range is also within 4 and 8 % of values obtained by Jourdan et al. [43] in non-stationary flows using accelerating and decelerating spheres with M_a values of 0.47 to 0.61 relative to the flow. Overall, good agreement was found between the measured values of C_d for the nine spheres and those from published sources.

Figure 9 shows the distribution of the pressure coefficient around the surface of the 4.5 mm spherical lead pellet (No. 1 in Fig. 2) that was measured as described in the previous section using the arrangement shown in Fig. 8. The values of pressure coefficient shown in Fig. 9 were calculated using the pressures measured at the pressure tapping hole, when the hole was located successively at various azimuthal angles, θ^o , between θ^o and θ^o (see Figs. 8 and 9). Figure 9 shows that the minimum pressure coefficient occurred at azimuthal angle θ^o of just less than θ^o , and that flow separation occurred at an angle of just less than θ^o , where the pressure coefficient recovery faltered due to the flow having separated from the pellet surface. These results are in good agreement with those found in published sources at subcritical values of Re. For example, Achenbach [28] found that with smooth spheres, laminar boundary layer separation occurred at θ^o where local skin friction tended to reduce to

zero. Son et al. [30] found that with almost negligible free stream turbulence, the minimum value of pressure coefficient occurred at 70.5° , while separation occurred at 80° . Similarly, Aoki et al. [5] found that the minimum value of pressure coefficient for several smooth spheres occurred at $\sim 74^{\circ}$.

The pressure coefficient distribution of Fig. 9 for the 4.5 mm spherical lead pellet was integrated numerically using Eq. (8), as described above, which gave a value of $C_d = 0.539$. The numerical integration was also carried out using Eq. (6) and as expected a $C_d = 0.543$ was obtained, which is nearly the same value obtained with Eq. (8). The value of $C_d = 0.539$ from pressure-area numerical integration is only different by 5.7 % from the value of 0.51 obtained independently using the load cell arrangements of Figs. 5 and 6 for the same pellet, at the same values of M_a and Re.

The value of C_d = 0.539 obtained from pressure-area numerical integration accounts for pressure drag only and does not include surface friction drag. Results in Achenbach [28] show that for smooth spheres, surface friction at Re ~ 55,000 would add approximately 2 % to the value of C_d obtained from pressure drag alone. This surface friction would increase the value of C_d to approximately 0.55 when using the pressure-area numerical integration. Therefore, the overestimate of C_d = 0.55 is approximately 8 % when compared with the value of C_d = 0.51 obtained with the load cell system, which includes implicitly both pressure drag and surface friction.

In Fig. 9 and in Figs. 10, 11 and 15 to be discussed later, the value of pressure coefficient at the stagnation point ($\theta = 0^{\circ}$) is a little greater than 1.0 (approximately 1.1), due to significant flow compressibility at $M_a \sim 0.6$. For compressible flow, Houghton et al. [44] derive the following expression between pressure coefficient at a stagnation point $C_{p_{stagn}}$ and free stream Mach number, M_a , as shown in Eq. (9):

$$C_{p_{stagn}} = 1 + \frac{M_a^2}{4} + \frac{M_a^4}{40} + \frac{M_a^6}{1600} + \cdots$$
 (9)

At a low free stream value of $M_a \sim 0$ corresponding to incompressible flow conditions, the stagnation pressure coefficient $C_{p_{stagn}}$ given by Eq. (9) is 1.0. This is also the value obtained

if the Bernoulli equation applicable to incompressible flow is used to derive an expression for $C_{p_{stagn}}$. However, at a fairly high free stream value of $M_a \sim 0.6$ used for the experiments in this paper, the value of $C_{p_{stagn}}$ given by Eq. (9) is 1.093, which is almost 10 % greater than unity.

Concluding this section, the measured values of C_d for spheres, obtained with the load cell and with pressure distribution methods, were in good agreement with published values at comparable values of free stream Re and M_a .

3.2 Pressure and drag force distributions around the dome-head pellet

Figure 10 shows the measured distributions of pressure coefficient and drag force around the dome-head pellet. Pressure coefficients are shown for 27 surface area bands labelled "a" to "aa" (see Fig. 7) around the dome-head pellet at Re \sim 54,000 and $M_a \sim$ 0.58. For information, the data of Fig. 10 have also been re-plotted in Fig. 11 but this time, following convention, the x-axis shows the axial distance (streamwise direction) from the pellet nose tip.

Figure 10 shows that the flow was brought to rest at the stagnation point at the centre of the pellet nose and as a result, the pressure coefficient for band "a" rose to just over 1.0. Further away from the stagnation point, close to the pellet head rim (area bands "g" and "h"), the pressure coefficient was close to its lowest value of approximately -0.6.

At the head rim, the flow velocity attained a high value and, as a result, the surface pressure reduced to a minimum (a more detailed discussion of the influence of nose shape on flow velocity follows in the next section). Between area bands "a" and "h", on the pellet front face, the pressure coefficient reduced progressively, as the flow velocity rose from zero at the centre of the nose to a high value at the pellet rim.

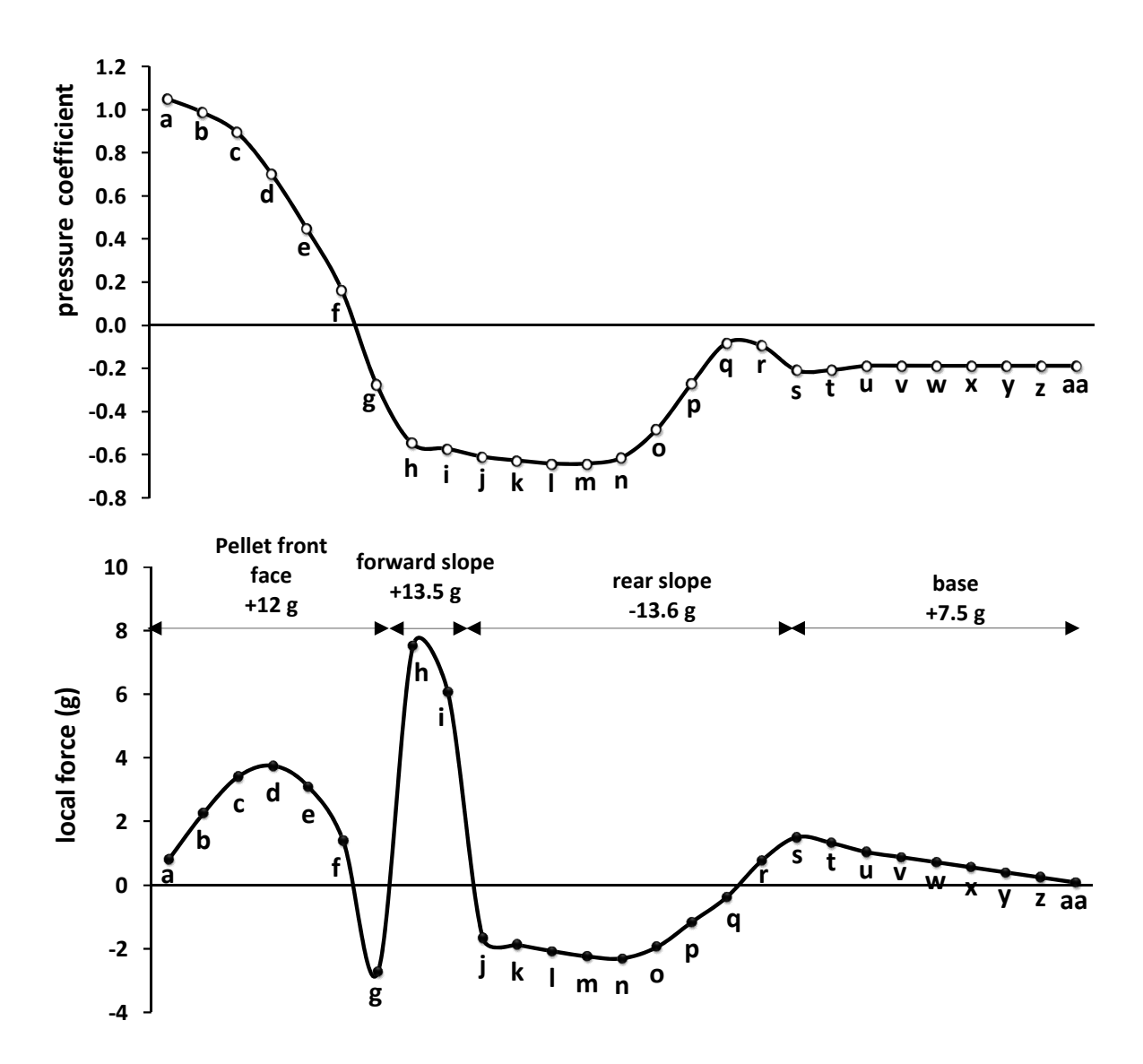
Downstream of area band "h", the pressure coefficient remained approximately constant at approximately -0.6 for six downstream area bands "i" to "n". This suggests that the flow boundary layer had separated from the surface of the pellet, somewhere close to the head rim (between surface area bands "g" and "h"), and had become a free shear layer. As the free stream flow was not in contact anymore with the pellet surface, it had no significant influence

on the surface pressure between bands "h" to "n". This was reflected in the pressure coefficient remaining approximately constant at -0.6.

The free shear layer that left the pellet at the head rim formed an interface between the high velocity free stream and a low-pressure recirculation region near the pellet surface between bands "h" and "n". Entrainment of fluid from this recirculation region into the layer maintained this region at low pressure.

Close to the pellet tail at band "n", the surface pressure begun to rise substantially. The pressure coefficient rose rapidly from approximately -0.6 at band "n" to -0.1 at band "r" on the pellet tail rim. This rise was caused by the shear layer impinging and re-attaching onto the pellet surface just downstream of area band "n". Figure 12 has been included in order to demonstrate that the rise in pressure observed experimentally in Figs. 10 and 11 after band "n" was due to flow re-attachment. Figure 12 shows that the shear layer detaching at the head rim subsequently re-attached onto the pellet surface near the tail, which agrees with the observations of Figs. 10 and 11, showing that the pressure coefficient value rose after surface band "n". Figure 12 was constructed for the dome and flat-head pellets using results obtained with Computation Fluid Dynamics (CFD) simulation (OpenFoam, free stream velocity 200 m/s, compressible rhoCentralFoam solver, RAS kOmegaSST turbulence model, mesh 1.1×10^6 cells). Figure 12 also confirms the presence of a recirculation zone behind the pellet base. From Fig. 10 it can be seen that the base of the pellet (bands "s" to "aa") lay within the rear recirculation region. As a consequence, the value of the pressure coefficient at the pellet base was approximately constant at approximately -0.2.

Figure 10 also shows the distribution of 27 local forces acting on the area bands "a" to "aa". All 27 forces shown in the figure were pressure forces on the bands and these forces were calculated and resolved axially as described previously. The sign convention for the forces, outlined in Fig. 10, is as follows: a positive local force (e.g. on band "d" on the front face) was a drag force that retarded the pellet (i.e. contributed to the overall drag force on the pellet), while a negative force (e.g. on band "m" on the rear slope) accelerated the pellet and thus



local drag force was based on measured local *gauge* pressure; +ve force ≡ drag in streamwise direction; -ve force ≡ force in counter-streamwise direction; 1 g force = 0.0098 N Note: the empty and filled data markers (o and o) correspond

Figure 10 Pressure coefficient and local drag force distributions around 4.5 mm calibre dome-head pellet (No. 2 Fig. 2) (Re \sim 54,000, $M_a \sim$ 0.58)

to area "bands" a, b, c, etc, not to the pressure tappings

reduced the overall pellet drag. The overall pellet drag was calculated by summing up (algebraically) all the local forces.

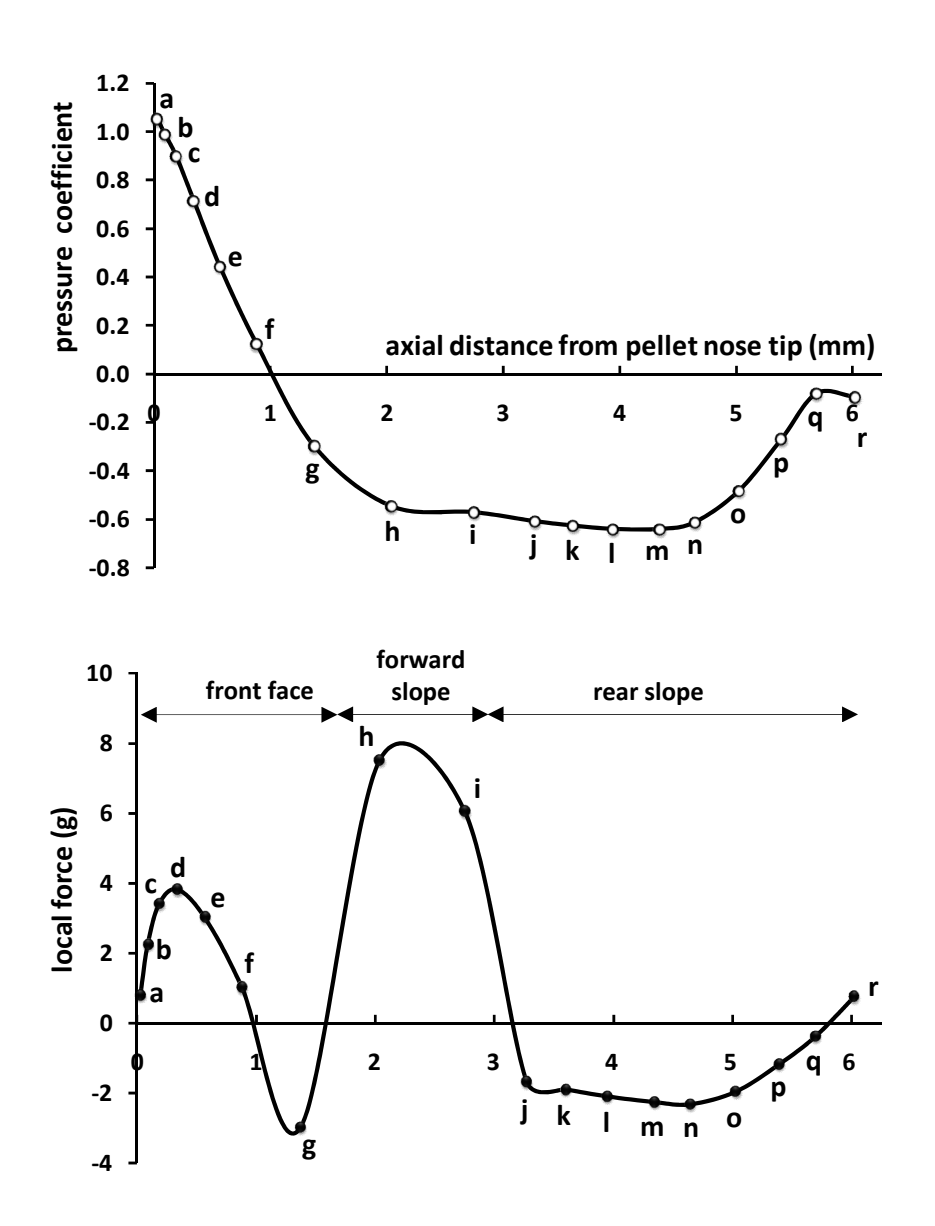


Figure 11 Pressure coefficient and local drag force distributions of Fig. 10 re-plotted but with x-axis showing the axial distance from the pellet nose tip (pellet base data are all at axial distance of 6.3 mm)

Figure 10 shows that the following forces contributed to drag and therefore retarded the pellet: aggregate band forces of +12 g (0.118 N) acted on the pellet front surface; aggregate of +13.5 g (0.132 N) acted on the forward slope; and aggregate of +7.5 g (0.074 N) acted on the pellet base. On the other hand, the band forces which tended to accelerate the pellet acted mostly on the rear slope and aggregated to a force of -13.6 g (0.133 N). Therefore, a total of 33 g of retarding forces was offset by 13.6 g of accelerating force, resulting in a net overall drag on the pellet of 19.4 g (0.19 N). It is interesting to note that for this pellet, the retarding force on the *forward slope* (13.5 g, 0.132 N) was almost entirely offset by the accelerating force on the *rear slope* (-13.6 g, 0.133 N). This meant that the retarding forces on the pellet

front face and on its base were the only two significant forces that decided the overall drag on the pellet. For this pellet, the front face contributed 61.9 % of the overall pellet drag and the base contributed 38.7 %.

An interesting observation from Fig. 10 is that the shear layer re-attachment on the pellet rear slope raised the pressure on bands "o", "p" and "q". At first thought, this pressure rise may appear to have been undesirable, as it curtailed the accelerating (-ve) force acting on the rear slope of the pellet. However, the re-attachment also raised the pressure at band "r" from which the flow once again detached from the pellet. The higher pressure at band "r" had the beneficial effect of also raising the pellet base pressure, which reduced base drag. Therefore, the loss of accelerating force on the rear slope was offset by lower decelerating force (drag) on the pellet base.

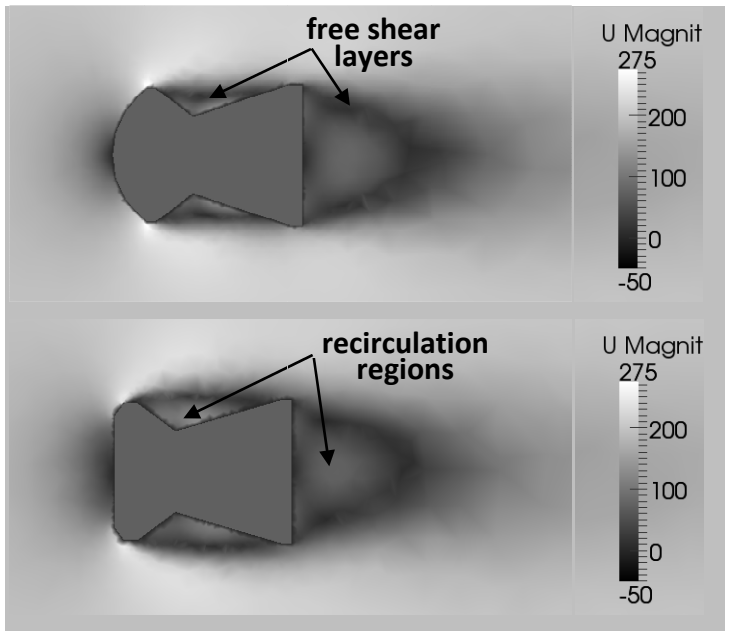


Figure 12 Predicted velocity fields (m/s) using Computational Fluid Dynamics for two 4.5 mm pellets (2 and 3, Fig. 2) at Re $\sim 54,000$, $M_a \sim 0.58$

The figures given above for the drag distribution around the pellet are subject to experimental error. While the overall pellet drag was estimated to be 19.4 g (0.19 N) using pressure-area integration, the overall pellet drag measured with the load cell system was 16.3 g (0.16 N), which is 16 % lower. Experimental errors arose from a number of sources, including the measurements of individual tapping holes pressure, alignment of pellet and flow, and precise measurement and control of freestream velocity head. While the quantitative results discussed

above require some caution, the qualitative discussion and the physical phenomena identified and discussed above are most likely to be correct.

Concluding this section it can be said that: (a) the dome-head pellet drag is dominated by the drag on its front face and its base, which contribute ~ 62 % and ~ 38 % respectively of the overall pellet drag; and, (b) the detailed behaviour of the separated boundary layers can affect the drag contributions made by the two side-slopes and by the base of the pellet.

3.3 Relationship between pellet nose shape and surface pressure

The preceding section concluded that the majority of overall drag on the dome-head pellet emanates from its front face (~ 62 %). This section considers in more detail how the geometry of the front face influences the pressure distribution on the face and thereby pellet drag. It does this with the help of two-dimensional (2-D) potential flow theory using Cartesian (x-y) co-ordinates. The theory is based on the conservation of fluid mass and momentum, expressed in differential form. A number of simplifying assumptions allow analytical solutions of the differential conservation equations. The solutions are algebraic expressions, which allow fluid velocity and pressure to be calculated at any location in the fluid surrounding the immersed 2-D shape. The conservation of mass provides the flow velocities, while the conservation of momentum provides the pressures by making use of the calculated velocities. The simplifying assumptions consider the flow to be incompressible, irrotational, and inviscid. The simplification of flow incompressibility is a significant departure from real flow behaviour at the fairly high Mach number of 0.58 at which experiments for this paper were conducted. It can be shown that at $M_a = 0.58$, a 1 % increase in flow velocity can cause a significant reduction in density of ~ 0.34 %. The other two simplifications of irrotational and inviscid flow are reasonable approximations away from the pellet surface, but depart significantly from reality close to the surface of a body. Owing to the assumptions associated with potential flow, it does not consider the thin boundary layer that exists in real flows close to the surface of the body. As a consequence, potential theory cannot predict flow separation, and is therefore useful only in regions where a real flow is attached to the solid body surface, but not in regions where a real flow is likely to separate. Because it is a simplified analysis, it will be seen from the following discussion that potential flow provides useful *physical insights* into how the shape of pellet nose can influence surface flow velocities and surface pressures and, thereby, pellet drag. Potential flow theory is

therefore used here as an aid to understanding but not as a predictive tool of complex flow behaviour. Computational fluid dynamics would be a more appropriate predictive tool, as it does not include major simplifying assumptions such as inviscid and irrotational flow and it can incorporate compressibility.

In the following discussion, a key relationship of potential flow theory is as shown in Eq. (10) [45]:

surface slope,
$$\frac{dy}{dx} = \frac{v}{u}$$
 (10)

where u and v are the components in the x and y directions of the surface flow velocity, V. Once the Cartesian velocity components u and v have been calculated from potential flow, [45] the resultant surface velocity, V, is obtained from Eq. (11),

resultant surface velocity,
$$V = \sqrt{u^2 + v^2}$$
 (11)

Then, the Bernoulli equation is used for the surface streamline as shown in Eq. (12),

surface pressure,
$$p_f = p + \frac{1}{2}\rho U^2 - \frac{1}{2}\rho_f V^2$$
 (12)

where p_f and ρ_f are the surface streamline pressure and density and p and ρ are the free stream values. Subject to assumptions stated above, the Bernoulli equation represents conservation of momentum and allows the surface pressure to be calculated after the surface velocity has been calculated from mass continuity.

Equation (10) implies that the surface velocity follows the body surface slope. This is true only in theory, as in real flows there is the presence of the boundary layer and surface no-slip condition which modify further the surface velocity. Furthermore, the flow may separate from the surface, in which case potential flow theory is no longer applicable.

Figure 13(a) shows five basic 2-D nose shapes labelled (i) to (v) together with streamlines drawn using potential flow. All five shapes have a maximum half-height of y = 2.25 mm but

different nose lengths; shapes (i) and (ii) are Rankine ovals, (iii) and (iv) Kelvin ovals, and (v) is 45° wedge. [45] Eight streamlines are shown which approach the shapes parallel to their axes at $y = \pm 0.10$, ± 0.33 , ± 0.66 , and ± 1.00 mm.

In physical terms, the pressures on the surfaces of the five shapes in Fig. 13(a) are caused by accelerations or decelerations of the flow at their surfaces. It is therefore important to examine how the surface geometry of the various shapes accelerates or decelerates the flow on its surface. This will be done, first, without considering the likelihood of flow separation, as this will emphasize the influence of body nose geometry on surface velocities and surface pressures. Then, the likelihood of flow separation will be considered, as could occur in real flows. Consider flows around two of the shapes with substantially different nose shapes, that is the oval-nose shape (i) and the flat-nose shape (iii) in Fig. 13(a). The resultant velocity, V, on their surface is shown in Figs. 13(b) and (c) respectively, together with the horizontal (u) and vertical (v) components of V. Figure 13(b) and (c) show two major differences in the surface velocity, V, for the two shapes. Firstly, close to the shape axes (y < 1.1 mm), the surface velocity of the oval-nose shape is larger than that for the flat-nose one. The lower velocity for the flat-nose shape is due to the free stream being brought almost to rest in the horizontal direction on the flat face (velocity component $u \sim 0$). This is not what happens with the oval-nose shape, which retains considerable proportion of its horizontal velocity component, u. Because the oval-nose shape has a higher velocity, V, near its axis (y < 1.1mm), it will experience a *lower pressure* than the flat-nose shape and therefore *lower drag* force near the axis. This is illustrated well in Fig. 14(a), where the pressure coefficients were calculated using the surface velocity and the Bernoulli Eq. (12). The pressure coefficient for the oval shape can be seen to be significantly lower for y < 1.1 mm. Returning to Fig. 13(b) and (c), consider now the surface velocity for the two shapes, further away from their axes, close to their rim (y > 1.75 mm). Figure 13(b) and (c) show that the situation has been reversed, and that the surface velocity for the oval-nose shape is now smaller than that for the flat-nose shape. It can be seen from the figure that this is because the oval-nose shape, with its much smaller surface slope, accelerates the flow vertically much less than the flat-nose shape does (vertical velocity component, v, smaller in the case of oval shape for y > 1.75mm). Because the oval-nose shape has a *lower resultant velocity*, V, near its rim (y > 1.75mm), it will also experience a *higher pressure* near its rim than the flat-nose shape. This is also shown in Fig. 14(a), where the pressure coefficient for

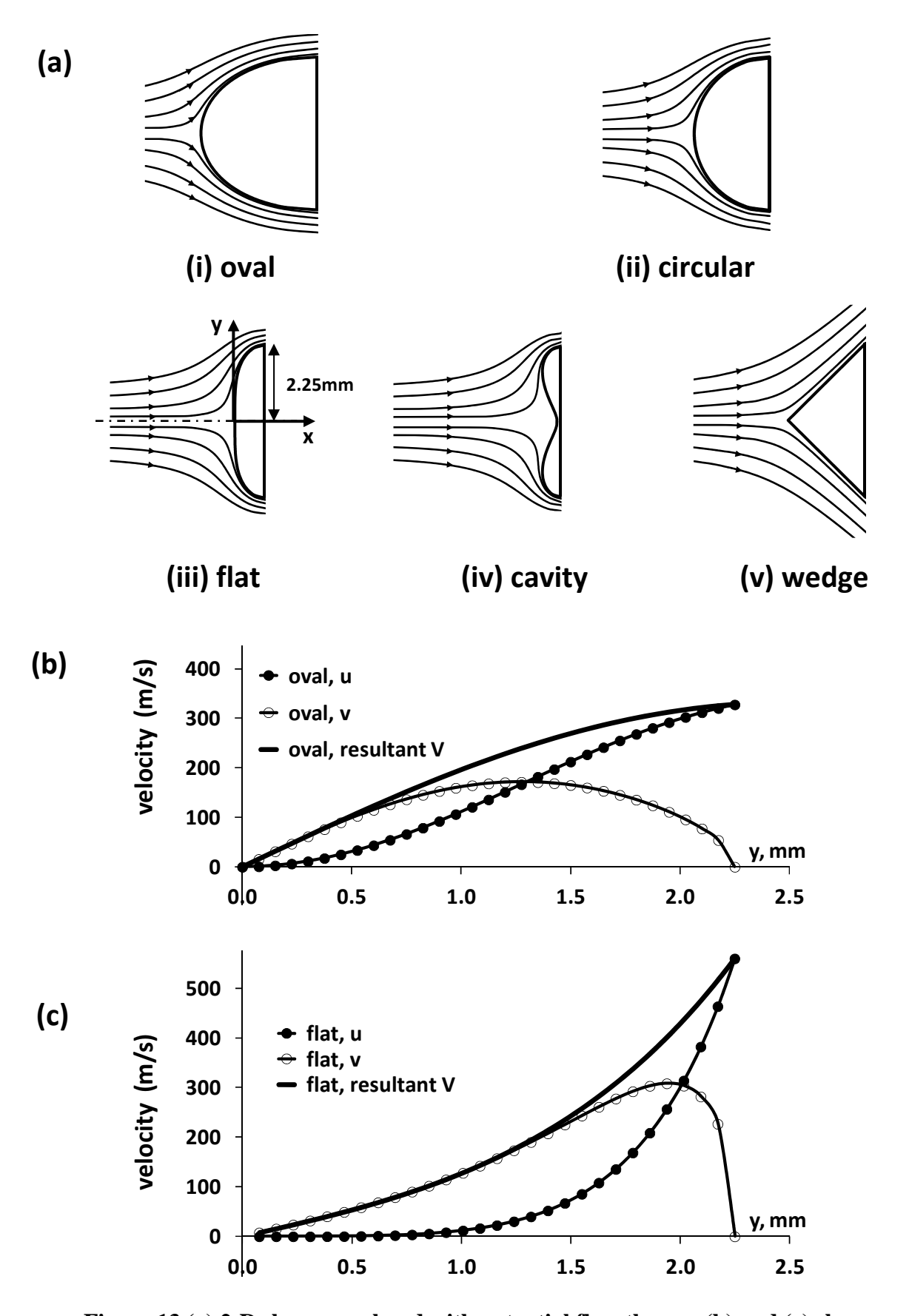


Figure 13 (a) 2-D shapes analysed with potential flow theory; (b) and (c) show calculated surface velocity components (u, v) and resultant velocity (V) for oval shape (i) and flat shape (iii) at $M_a \sim 0.58$ and $Re \sim 54,000$ (free stream velocity 200 m/s)

the oval-nose shape is significantly higher (less negative) for y > 1.75 mm than that for the flat-nose shape.

In the absence of flow separation prior to the flow reaching the rim, the flat-nose shape would have a theoretical advantage of very low negative pressure coefficient close to the nose rim (y > 1.75 mm). The low sub-atmospheric pressure *near the rim* would result in greater accelerating force acting near the rim in the *counter-streamwise direction*. This accelerating force would tend to offset the drag in the *streamwise direction* that occurs at the *inner portion* (y < 1.1 mm) of the flat-nose shape. It can be shown, using pressure-area integration, that the negative pressure coefficients near the rim of the flat-nose shape offset the positive pressure coefficients near the centre of the shape, theoretically resulting in zero overall net drag force on the nose.

However, with real flows, this does not occur in practice, and a substantial drag force always exists on the front face of real pellets. This is due to the existence of the surface boundary layer on the pellet front faces plus the likelihood of flow separation close to their rim, which prevent very low negative values of pressure coefficient occurring on the front faces of real pellets. This situation is evident in Fig. 9 in the case of the spherical lead pellet, where flow separation occurs ahead of the spherical pellet apex and at a fairly moderate negative value of the pressure coefficient of -0.36.

Returning briefly to the five shapes of Fig. 13(a), with real flows the likelihood of flow separation upstream of the nose rim would be significant in bodies having profiles such as those of the flat-nose shape (iii) and some of the other shapes, such as the circular-nose one (ii) and cavity-nose shape (iv).

Setting aside for a moment flow separation, the pressure coefficient curves of Fig. 14(a) provide some useful physical insights of how nose geometry affects surface pressure. Figure 14(a) shows that the flat nose body has a much lower theoretical value of pressure coefficient at the body rim (y = 2.25 mm) than the oval-nose shape. This low value of the coefficient for the flat-nose shape is due to greater curvature of the streamlines around the rim of the flat-nose, when compared with the curvature for the oval-nose shape, as can be seen from Fig. 13(a)(i) and (iii). Close to the rim, the flow has to turn over a greater angle in the case of the

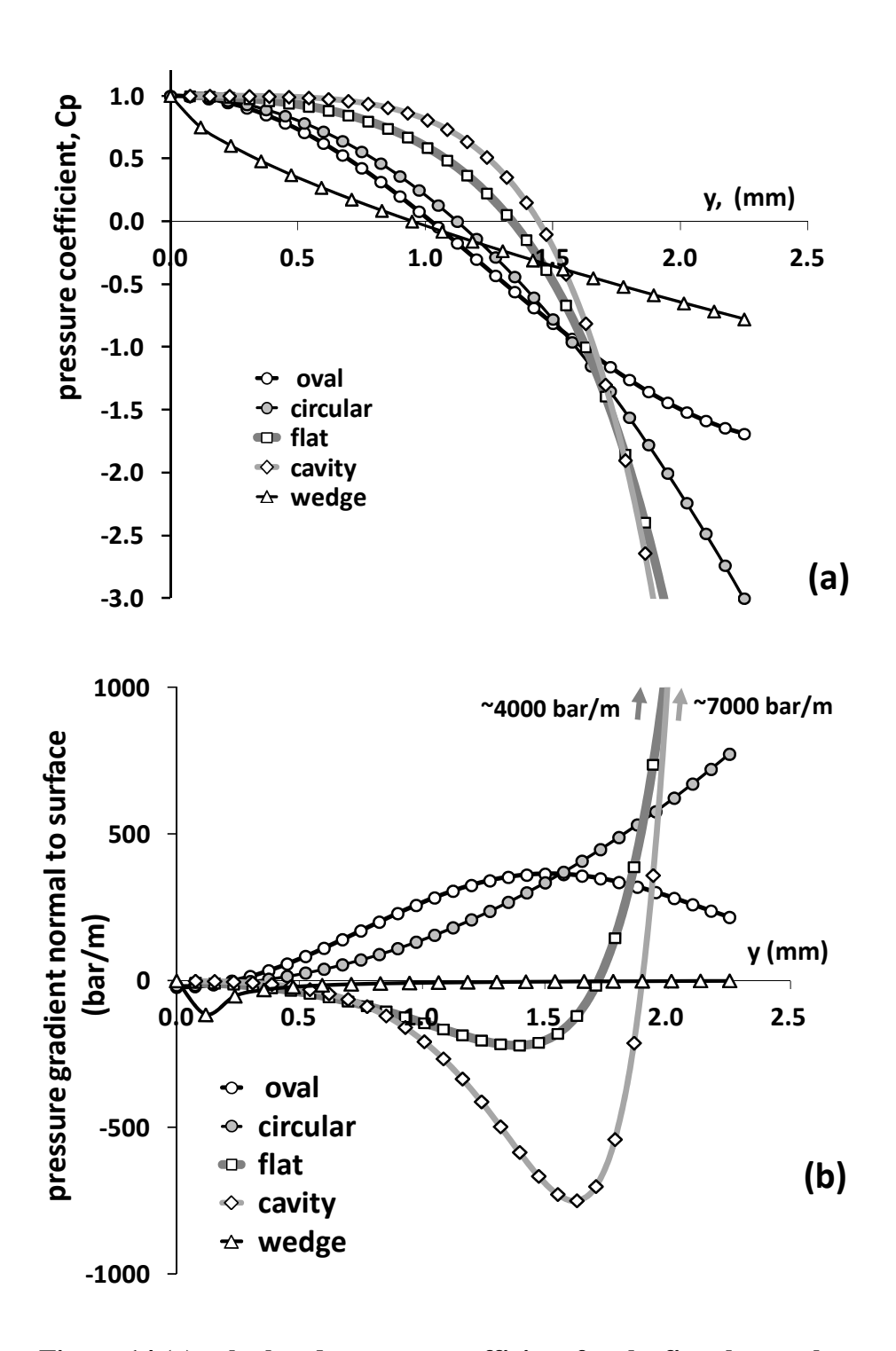


Figure 14 (a) calculated pressure coefficient for the five shapes shown in Fig. 13(a) at $M_a \sim 0.58$ and $Re \sim 54,000$; (b) Calculated pressure gradient normal to the surface (across 0.1 mm from surface)

flat-nose shape. This requires substantially higher centripetal acceleration at the rim of the flat-nose shape in order to ensure radial equilibrium of the fluid elements as they flow past its rim. In turn, this higher centripetal acceleration needs to be provided by a high pressure

gradient normal to the rim surface. As the free stream pressure is constant and at atmospheric level, the high pressure gradient can only be generated by a very low surface pressure at the rim of the flat-nose shape. This is entirely consistent with the very high flow velocity of 600 m/s and the very low pressure coefficient at the rim of the flat-nose shape. Figure 14(b) illustrates this point, and it shows the pressure gradient normal to the surfaces of the various shapes, calculated across 0.1 mm from the surface. The figure confirms the much greater pressure gradient required for the flat-nose shape for radial equilibrium at the rim (y = 2.25)mm); the normal pressure gradient for the flat-nose shape is ~ 7000 bar/m compared with ~4000 bar/m for the oval-nose one. Considering flow separation, the presence of a boundary layer in real flows introduces the likelihood of separation close to the rim for several of the nose shapes shown in Fig. 13(a). The likelihood of separation is greater for shapes requiring high radial pressure gradients near the rim in order to keep the flow attached, such as the flatnose and cavity-nose shapes. Incidentally, the values of negative pressure coefficient near the rim shown in Fig. 14(a) for the various nose shapes are very low in comparison to the measured values for the spherical lead pellet (Fig. 9) and the dome-head pellet (Fig. 10) which show pressure coefficient values of -0.4 to -0.6. Much of this difference is because the spherical and dome-head pellets are three dimensional bodies and allow "flow relieving" compared with the 2-D shapes of Fig. 13(a) [45]. Similar flow relieving also occurs in real flows. For example, the minimum value of C_p for 3-D flow occurring around a sphere is -0.55 (incompressible flow, Re 55,000 to 162,000 [28]), while the minimum value of Cp for 2-D cross-flow past a long cylinder is considerably lower at -1.15 (incompressible cross-flow, Re 54,000 to 129,000 [46]).

Although not discussed in great detail, the physical principles discussed above apply also to the other shapes (ii), (iv) and (v) shown in Fig. 13(a).

3.4 Comparison of pressure distribution and drag for four pellets

Figure 15 compares the measured pressure and drag distributions around four pellets at Re of approximately \sim 54,000 and $M_a \sim$ 0.58. All four pellets had 4.5 mm head diameter and the following front face profiles: dome-shaped (No. 2), flat-shaped with a rim chamfer (No. 3), conical-shaped (No. 4) and conical-shaped with an extensive central cavity (No. 5).

Figure 15 shows that compared with the other pellets, the flat-head pellet had high values of pressure coefficient extending over 74 % of pellet front face area, from band "a" to band "f" (r = 0 to 1.93 mm). The reasons for the high values of coefficient were discussed in the previous section. The cone-head pellet (apex half-angle 45°) had the lowest pressure coefficient values over 33 % of its face area, from band "a" to "d" (r = 0 to 1.29 mm). The cavity-head pellet was almost identical to the cone-head pellet, except for the presence of the head cavity (see pellets 4 and 5 and lower part of Fig. 2). This pellet had the highest values of the coefficient close to the pellet axis (over 18 % of its face area), corresponding to area bands "a" to "c" (r = 0 to 0.96 mm), all of which were inside the cavity. Outside the cavity from area band "d" outwards, the coefficient value fell very rapidly to approximately similar values as those for the cone-head pellet, which was expected as the cavity and cone-head pellets were almost identical apart from the presence of the cavity. Incidentally, Fig. 15 shows an inflexion in the curve for the cavity-head pellet between area bands "d" and "f" (reproduced in 3 repeated experiments). It is suggested that this was due to reversed flow leaving the cavity and detaching temporarily over the cavity lip, but subsequently reattaching a short distance downstream onto the sloped pellet surface. Next, considering the dome-head pellet, the pressure coefficient level very close to the pellet axis (bands "a" and "b", r = 0 to 0.64 mm) was high, due to the nearly flat face there. Away from the axis (beyond band "d") toward the head rim, the coefficient declined rapidly.

Returning to Fig. 15, it can be seen that for all four pellets, the flow separation occurred somewhere between bands "g" and "h". After flow separation, the value of the pressure coefficient for all four pellets remained almost constant for a long distance downstream, from band "h" all the way to band "n". Pressure recovery begun around band "n" due to impingement and re-attachment of the shear layer onto the rear slope of the pellet. Figure 15 suggests that the value of the pressure coefficient at the *detachment point* (between bands "g" and "h") affected the downstream location where the flow re-attached onto the pellet tail surface. For example, Fig. 15 shows that in the case of the dome-head pellet, re-attachment occurred relatively early at area band "n", while for the cavity-head pellet, re-attachment occurred two area bands downstream at "p". Therefore, Fig. 15 suggests that re-attachment and pressure recovery occurred earlier when the value of the coefficient at the upstream detachment point was low. A physical explanation for this observation can be proposed with the help of Fig. 12. The free shear layer, detaching from the pellet head rim, is subjected to a radial pressure gradient because the free stream is at atmospheric pressure, while the forward

recirculation zone is at lower, sub-atmospheric pressure. This causes the shear layer to curve toward the pellet axis and move closer to the pellet surface. As a result, the impingement point onto the rear pellet slope is also further upstream. This is what appears with the domehead pellet, where the lower pressure in the recirculation zone intensified the radial pressure gradient on the shear layer, increasing its curvature and causing it to impinge earlier onto the pellet sloped tail, around band "n". In the case of the cavity-head pellet, for which Fig. 15 shows a higher pressure within the recirculation region, the converse is true and shear layer re-attachment occurred later, around band "p" (see Fig. 15).

Figures 12 and 15 show that flow detached again at the tails of the four pellets, between area bands "q" and "r". Close examination of Fig. 15 suggests a link between the pressure coefficient at the two flow detachment points, at the pellet head and tail rims. The value of the pressure coefficient at the head rim appears to relate to the value of the coefficient at the tail rim. For example, the dome-head pellet had the lowest value for the coefficient at bands "g" and "h", but at the tail band "r" its coefficient value was highest. Conversely, the cavityhead pellet had the highest coefficient value at bands "g" and "h" but the lowest value at band "r". There was therefore an inverse relationship between the values of the pressure coefficient at the two detachment points. This is confirmed by an almost perfect Pearson correlation coefficient of -0.976 between the pressure coefficients at the head bands "h" and the tail bands "r" (Pearson correlation coefficient values are quoted in the rest of this paper). The boundary layer detaching from the pellet tail (between bands "q" and "r") became a free shear layer, which engulfed a large, low pressure, recirculation region behind the pellet base. As shown in Fig. 15, the pressure within the recirculation region was sub-atmospheric, while that of the free stream was atmospheric. The free shear layer was therefore subjected to a radial pressure gradient, which caused it to curve toward the pellet axis and enclose the rear recirculation region, as shown in Fig. 12. Figure 15 suggests that the pressure within this recirculation region had a positive relationship with the pressure at the tail detachment point. For example, the dome-head pellet had the highest coefficient value at area bands "q" and "r" and the highest average coefficient value for area bands "s" to "aa". Similarly, the cavityhead pellet had the lowest coefficient value at area bands "q" and "r" and lowest average value for area bands "s" to "aa". In fact, for the four pellets, a high positive correlation coefficient of 0.924 was calculated between the averaged pressure coefficient at bands "q" and "r" and the averaged coefficient at bands "s" to "aa".

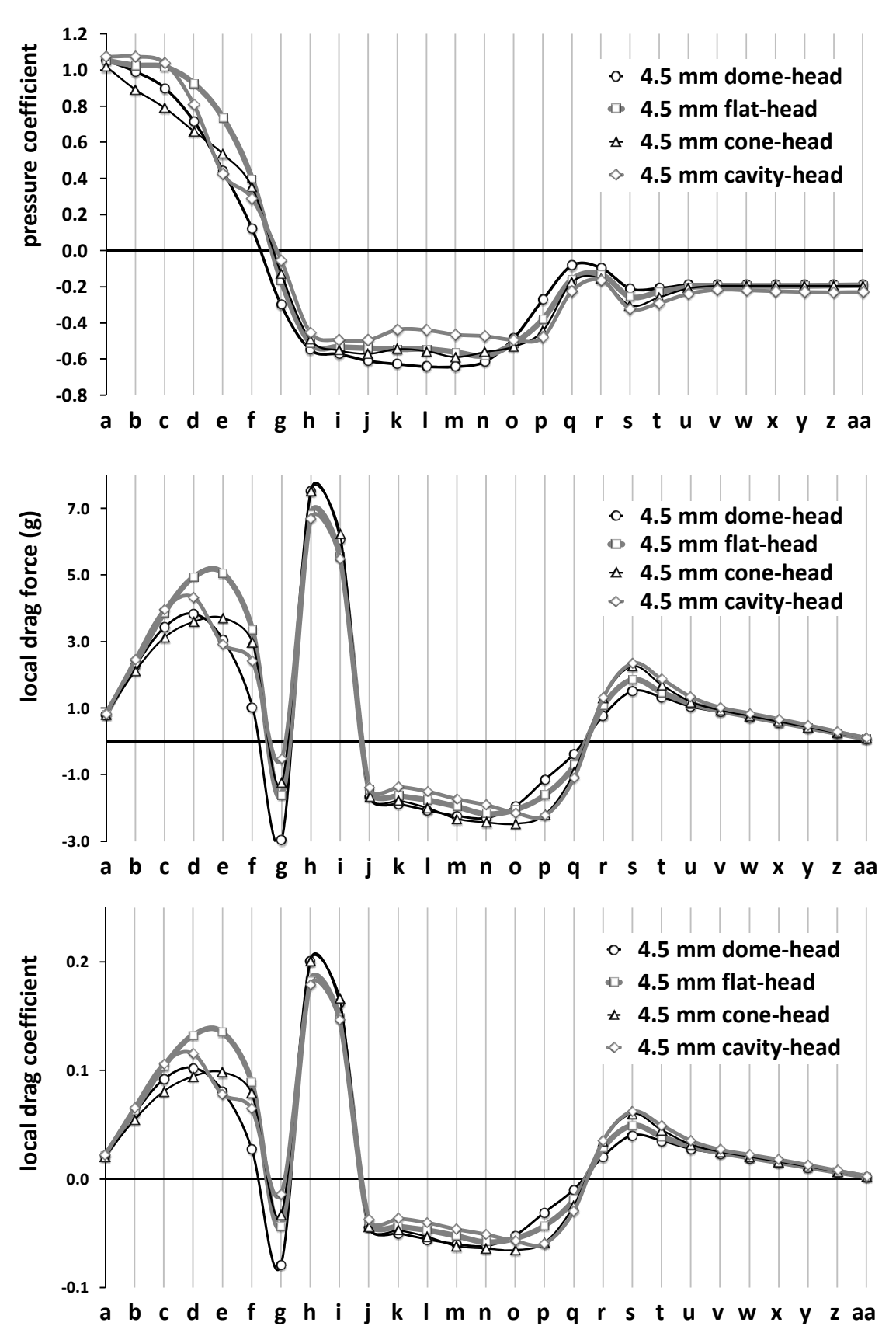


Figure 15 Pressure coefficient, local drag force, and local drag coefficient distributions around four 4.5 mm calibre pellets at Re \sim 54,000, $M_a \sim$ 0.58 (Pellets No 2 to 5, Fig. 2) (a, b, c, etc., are pellet surface area bands shown in Fig. 7)

So far, the results in Fig. 15 have been discussed mostly in terms of the pressure distribution around the four pellets. Figure 15 also shows the distributions of *local drag force* and *local drag coefficient* around each pellet. The local drag coefficient is defined by Eq. (13),

$$local \ drag \ coeffcient = \frac{local \ drag \ force}{\frac{1}{2}\rho U^2 \ A}$$
 (13)

where *local drag force* is the drag force for any local area band (band "a", "b", etc.), A is the cross sectional area at the *pellet head rim*, and $\frac{1}{2}\rho U^2$ is the free stream velocity head. Equation (13) provides the *local drag coefficient* for any pellet surface area band, calculated using the local drag force and the pellet cross sectional area at the head rim. As mentioned previously, if the local drag forces and the local drag coefficients for the 27 surface area bands are summed up algebraically, the overall drag force and overall drag coefficient for a pellet as a whole are obtained. Table 2 was constructed using the local drag coefficients. For each pellet, Table 2 breaks down the pellet overall drag coefficient into four pellet regions: the front face, forward and rear slopes, and pellet base. It is more convenient to first consider the drag coefficient contributions of the forward and rear pellet slopes. For all four pellets, Table 2 shows that the drag force on the forward slope was offset almost entirely by the drag force on the rear slope. Quantitatively, the *net contribution* of the two slopes toward the overall drag coefficient for each pellet was -2 %, -4 %, -8 %, and -4 % for the dome-head, flat-head, cone-head and cavity-head pellets, respectively.

The *net influence* of the two side slopes on the overall drag was small due to several (interrelated) factors. Firstly, despite the rear slope having a greater projected area (normal to the pellet axis) than the forward slope, some of this larger area was rendered less important due to pressure recovery as a result of shear layer re-attachment close to the pellet tail (see Fig. 15). Secondly, a lower pressure on the rear slope did not automatically lead to a reduction in drag because the lower pressure also encouraged earlier pressure recovery, which reduced rear slope area on which the low pressure acted.

Table 2 shows that the overall pellet drag coefficient was made up almost entirely of the drag forces on the face of the pellet and on its base, with the former contributing 61 - 71 % of the pellet overall drag and the base contributing 32 - 42 %, depending on individual pellet

geometry. Examining the values of C_d for the *front face* of the four pellets, it can be seen that the greatest value of C_d was 0.50 for the flat-head pellet, followed by 0.44 for the cavityhead, 0.40 for the cone-head and 0.31 for the dome-head pellet.

Table 2 Breakdown of drag coefficient, calculated from pressure-area integration, into principal pellet regions for 4.5 mm calibre pellets at constant $Re \sim 54,000 \text{ and } M_a \sim 0.58$

pellet			calculated front slope C _d				calculated base C _d		calculated OVERALL PELLET Cd	error in C _d	
	$C_d^{(c)}$	% ^(d)	C _d	%	C_d	%	C_d	%	C _d	% ^(e)	
dome-head (2) ^(a)	0.31	61	0.36	72	-0.36	-72	0.20	40	0.503	19.2	
flat-head (3)	0.50	71	0.33	47	-0.36	-51	0.23	32	0.699	24.6	
cone-head (4)	0.40	67	0.36	61	-0.42	-70	0.25	42	0.597	-10.6	
cavity-head (5)	0.44	64	0.32	48	-0.36	-53	0.27	40	0.678	-5.0	

Notes: (a) pellet serial number in Fig. 2; (b) all values of C_d in this Table were calculated from pressure-area integration using information in Fig. 7 and the data plotted in Fig. 15; (c) C_d for pellet region (regions are: front face, front slope, rear slope, base as shown in Fig. 10) - C_d obtained by summing up algebraically individual area "band" values in Fig. 15(c); (d) region C_d as a percentage of the calculated OVERALL PELLET C_d ; (e) % error in calculated OVERALL PELLET C_d value compared with value measured directly using load cell system shown in Figs. 5 and 6

Table 2 shows also the variation in C_d for the pellet bases. The greatest value of 0.27 was for the cavity-head, followed by 0.25 for the cone-head, 0.23 for the flat-head pellet and 0.20 for the dome-head pellet. These results correlate positively and highly with the pressure coefficient at the head rim; in fact there is a +0.99 correlation coefficient between the base C_d for the four pellets and their pressure coefficients at the head rim separation point (i.e., average for bands "g" and "h"). However, only a fairly weak relationship was found between the value of C_d for the front face and the C_d for the pellet base (correlation coefficient 0.55). Table 2 shows that the value of C_d for the front face varied considerably between the four pellets, by 61 % between the smallest and largest values, while the value of C_d for the base varied less, by 35 %. Lastly, the overall values of C_d for the four pellets correlated very highly with the values of C_d for the front faces (correlation coefficient +0.97) and moderately with the C_d values for the bases (correlation coefficient +0.68). This could be expected as the

values of C_d for the front face dominated the overall pellet C_d by contributing ~ 65 % toward the overall pellet C_d values.

Concluding this section it can be said that the overall value of C_d for the four pellets was controlled almost entirely by the drag on the pellet front face and that on the base, with the front face accounting for approximately 65 % of the overall pellet drag. The results suggest that for low pellet face drag, the shape of the face close to the pellet axis needs to minimise the deflection (rotation) of the approaching free stream away from the pellet axis. This tends to minimise flow deceleration axially and also minimise flow acceleration transversely, both of which encourage low surface pressure and low drag near the axis of the pellet face. For example, an improvement in C_d for the cone-head pellet might be obtained with a smaller apex half-angle than 45°. The analysis of Salimipour et al. [4] demonstrated that optimisation of pellet nose shape requires a holistic approach which takes into account changes in pellet mass and muzzle velocity, in addition to in-flight changes in drag coefficient. Furthermore, pellet modifications should be assessed over the entire pellet flight range, using criteria such as minimising altitude drop and maximising ratio of pellet momentum at target/altitude drop. With this approach, Salimipour et al. show, for example, that the optimum cone half-angle for a 4.5 mm calibre cone-head pellet is 45° for minimum altitude drop over 35 m range, and 42° for maximum ratio of pellet momentum at target/altitude drop.

3.5 Comparison of pellet overall drag coefficient

The load cell system of Figs. 5 and 6 was used to measure the drag coefficient of the five pellets at Re $\sim 54,000$ and $M_a \sim 0.58$. The values obtained are shown below in Table 3:

Table 3 Comparison of values of drag coefficient measured with load cell system for the five 4.5 mm calibre pellets at Re $\sim 54,000$ and $M_a \sim 0.58$

pellet	sphere	dome-head	flat-head	cone-head	cavity-head
C_d	0.510	0.422	0.561	0.668	0.714
% difference from sphere	0	-17	10	31	40

It can be seen from these figures that the dome-head pellet had a 17 % smaller value of C_d than that for the spherical pellet. An analysis of the surface pressure coefficient distributions for these two pellets (Figs. 9 and 15) indicated the reasons behind this observation.

Considering, first, the face drag for the two pellets, the dome-head pellet had significantly higher face drag, indicated by *face* C_d of 0.31 compared with *face* C_d of 0.19 for the spherical pellet. Turning now to the base drag, there was strong reversal; the dome-head pellet had a much lower value of *base* C_d of 0.20 compared with *base* C_d of 0.36 for the spherical pellet. It appears, therefore, that the much lower base drag for the dome-head pellet more than offset its higher face drag, resulting in the overall C_d for the dome-head pellet being 17 % less than that for the spherical pellet. Reflecting on these results, it was apparent that the tail of the dome-head pellet was a key reason for its relatively low base drag. The key role of the tail was confirmed experimentally by removing the tail from the dome-head pellet, as shown in the lower part of Fig. 2, and measuring the value of C_d for the truncated pellet. Without the tail, the overall value of C_d climbed from 0.422 to 0.730, which was an increase of 73 %. It was apparent that the presence of the tail in the dome-head pellet enabled flow reattachment and a rise in base pressure, and this reduced its base drag. In contrast, at the value of Re \sim 54,000, flow reattachment on the rear surface of the spherical pellet was not possible, and for this reason, its base drag was higher than that for the dome-head pellet.

The flat-head, cone-head, and cavity-head pellets had larger *overall* C_d values than the spherical pellet, by 10 %, 31 % and 40 %, respectively. This was due to the three pellets having much larger face drag than the spherical pellet. The values of *face* C_d for the three pellets were 0.50, 0.40 and 0.44, respectively, compared with only 0.19 for the spherical pellet (Table 2 and Figs. 9 and 15). Turning now to the base drag, all three pellets had smaller values of *base* C_d than the spherical pellet (0.23, 0.25 and 0.27, versus 0.36). However, the *base* C_d values for the three pellets were not sufficiently smaller to compensate for their much larger values of *face* C_d . So, the three pellets ended up having larger overall C_d values than the spherical pellet.

A somewhat unexpected result was the 19 % larger *overall* C_d value for the cone-head pellet (0.668) compared to the value for the flat-head pellet (0.561) at the flow conditions of Re~54,000 and M_a ~ 0.58. The measurements and analysis were repeated with approximately the same C_d values being obtained. Rafeie and Teymourtash [2] analysed the aerodynamic and dynamic behaviours in flight of three 4.5mm calibre pellets in transonic compressible flow, with flow analysis being carried out using computational fluid dynamics. Two of the three pellets had similar (but not precisely the same) shapes to those of the flat-head and cone-head pellets being discussed here. At the Mach number of M_a = 0.58, the data [2] agree

with the data here, and they show that the cone-head pellet in the previous study [2] had a larger value of overall pellet C_d than the flat-head pellet, by approximately 8 %. However, this reversed at higher values of M_a greater than 0.65, where the flat-head pellet in the study [2] had a larger value of C_d than the cone-head pellet. Recently, Salimipour et al. [4] reported an extensive analysis of aerodynamic and dynamic behaviour in flight of four 4.5 mm calibre pellets, with the flow analysis being carried out using compressible three-dimensional computational fluid dynamics. Of the four pellets, two had similar head shapes to the two of the pellets being discussed here. One pellet had a flat-head shape similar to pellet 3, and a second pellet had a cone-head shape similar to pellet 4. The analysis in Salimipour et al. spanned a range of Mach numbers which were, however, higher than the value of $M_a \sim 0.58$ used for the experimental results being discussed here. The smallest Mach numbers shown in the previous study were $M_a \sim 0.64$ for the flat-head pellet and 0.75 for the cone-head pellet. On the whole, the data from Salimipour et al. suggest that at a somewhat greater value of M_a, the value of C_d for flat-head pellet was greater than that for the cone-head pellet. Future work by the author will examine the values of C_d for the cone-head and flat-head pellets over a wide range of values of Re and M_a.

4 Conclusions

A low turbulence jet with a nominal diameter of 17 mm proved to be a suitable facility for investigation at $M_a \sim 0.6$ of drag forces on small spheres and air rifle pellets having diameters in the range of 3 to 4.5 mm. The small drag forces involved required careful calibration and system set-up to achieve satisfactory repeatability and accuracy of the measured values of drag coefficient.

At $M_a \sim 0.6$, the behaviour of a small 4.5 mm spherical pellet proved to be very similar to widely published behaviour for spheres being a value of $C_d \sim 0.5$, which was independent of Re in the range 37,000 to 57,000, and flow separation at azimuthal angle of $\sim 78^\circ$.

The overall drag of four non-spherical pellets was dominated by the drag on their front face. The face contributed approximately 65 % of the overall pellet drag, while base drag contributed almost all of the remaining 35 %. The *net drag contribution* of the two side slopes of the pellets was close to zero.

The theoretical analysis of 2-D nose shapes and the measured drag distributions for five pellets showed that a streamlined pellet nose could, in theory, reduce the drag generated on the front face. However, this effect would mostly be limited to a central region of the front face, close to the pellet axis. The results of the theoretical potential flow analysis can only be indicative, as they assume incompressible and inviscid flow and do not allow the prediction of flow separation. In real pellets, flow separation near the rim of the front face can substantially affect the drag on the pellet face and also the base drag, as the pellet base is engulfed in the wake formed as a result of flow separation.

The geometry of the front face has a weak influence on the drag acting on the pellet side slopes and its base. This influence was exercised through the behaviour of the free shear layer separating from the pellet head rim. However, only a weak relationship was found between the value of C_d for the front face and the value of C_d for the pellet base (correlation coefficient 0.55).

Detailed theoretical and experimental studies suggested that for low pellet face drag, the pellet nose shape should be such as to minimise rotation of the approaching free stream away from the pellet axis. That is, it is necessary to minimise flow *deceleration* axially and also minimise flow *acceleration* transversely. Therefore, pellet nose shapes with spherical, ogive, or ellipsoidal nose geometries are likely to have smaller face drag than flat-head or cavityhead pellets.

The dome-head pellet was found to have 17 % lower overall C_d than the spherical pellet, likely due to the much lower *base drag* in the case of the dome-head pellet, which more than compensated for higher dome-head *face drag*. It was apparent that the presence of the tail in the dome-head pellet enabled flow reattachment and a rise in base pressure, thus reducing its base drag. In contrast, at Re \sim 54,000, flow reattachment on the rear surface of the spherical pellet was not possible, and it is likely that because of this reason its base drag was higher than that for the dome-head pellet.

The flat, cone, and cavity-head pellets had higher *overall* C_d values than the spherical pellet, by 10 %, 31 % and 40 %, respectively. It was shown that this was due to their having substantially higher face drag, which was not compensated sufficiently by their lower base drag.

When the value of C_d for a pellet was measured with the load cell system, the repeatability of the value was 1.3 % and the error in the value of C_d was estimated by means of uncertainty analysis to be 4.2 %. On the other hand, when the value of C_d was calculated from pressure distribution around the pellet, the error estimated by means of uncertainty analysis was considerably larger at 12.2 %.

Declaration of conflicting interest

The author declared no potential conflicts of interest with respect of the research, authorship, and/or publication of this article.

Funding

This research received no specific financial support from funding agencies in the public, commercial or not-for-profit sectors.

List of Symbols

A pellet cross sectional area at the pellet head rim

A_d area of pellet surface band "d"

 C_d Drag coefficient, $\frac{drag \ force}{\frac{1}{2}\rho U^2 \ A}$

CM centre of mass

CP centre of pressure

 C_p pressure coefficient, $\frac{p_s - p}{\frac{1}{2}\rho U^2}$

 $C_{p_{stagn}}$ pressure coefficient at a flow stagnation point

F_D overall pellet net drag force

F_d pressure force acting *normal* to pellet surface at surface area band "d"

F_{dx} pressure force at surface band "d" resolved in pellet axial direction

i.d. internal diameter

M_a jet or free stream Mach number

Ø diameter

o.d. external diameter

p jet or free stream static pressure (equal to p_a)

p_f surface streamline pressure

p₄, p₅ pressure at tappings 4, 5, at either side of pellet surface band "d"

p_a atmospheric pressure

p_s surface pressure used for calculation of pressure coefficient

 p_d mean pressure at surface area band "d", $p_d = \frac{p_4 + p_5}{2}$

p_o jet or free stream stagnation pressure

p_{oo} stagnation pressure just upstream of the entry to jet nozzle contraction

r radial distance from pellet axis

r₄, r₅ radial distance from pellet axis of pressure tappings 4, 5

R specific gas constant for air

R² multiple regression coefficient

Re Reynolds number

T jet or free stream static temperature

T_{oo} stagnation temperature just upstream of the entry to jet nozzle contraction

U jet or free stream velocity along nozzle axis
u flow velocity component along x direction

v flow velocity component along y direction

V resultant velocity whose components are u and v

x, y Cartesian co-ordinates (x for streamwise direction)

Greek symbols

γ ratio of specific heat capacities for air

 $\Delta\theta$ increment in azimuthal angle θ between successive pressure measurements

 θ azimuthal angle for the spherical lead pellet

ρ jet or free stream density

 $\rho_{\rm f}$ surface streamline density

References

- 1. House of Commons Home Affairs Committee. Third Report Session 2010-2011, Volume 1. UK House of Commons; 20 December 2010. Report No.: HC 447-I.
- 2. Rafeie M, Teymourtash A. Aerodynamic and dynamic analyses of three common 4.5 mm-caliber

- pellets in a transonic flow. Scientia Iranica B. 2016; 23(4): p. 1767-1776.
- 3. Corey K. Airgun pellet performance using computational fluid dynamics. MSc Thesis. College of Engineering, Rochester, Mechanical Engineering; 1994.
- 4. Salimipour S, Teymourtash A, Mamourian M. Investigation and comparison of performance of some air gun projectiles with nose shape modifications. J Sports Engineering and Technology. First Published Online March 4, 2018. DOI: 10.1177/1754337118759159.
- 5. Aoki K, Muto K, Okanaga H, al e. Aerodynamic characteristic and flow pattern on dimples structure of a sphere. In FLUCOME 2009, 10th International Conference on Fluid Control, Measurement, and Visualisation; 17-21 August 2009; Moscow. p. 1-10.
- 6. Cooke A. Shuttlecock aerodynamics. Sports Engineering. 1999; 2: p. 85-96.
- 7. Alam F, Chowdhury H, Moria H, al e. A comparative study of football aerodynamics. In 8th Conference of the International Sports Engineering Association (ISEA); 12 16 July 2010; Vienna, Austria.
- 8. Hong S, Asai T. Effect of area band shape of soccer ball on its flight characteristics. Scientific Nature, Scientific Reports. 2014; 4: 5068: p. 1-7.
- 9. Alaways L. Aerodynamics of the curve-ball: an investigation of the effects of angular velocity on baseball trajectories. PhD thesis. University of California Davis, USA; 1998.
- 10. Mehta R, Alam F, Subic A. Review of tennis ball aerodynamics. Sports Technol. 2008; 1: p. 7–16.
- 11. Ou K, Castonguay P, Jameson A. Computational Sports Aerodynamics of a Moving Sphere: Simulating a Ping Pong Ball in Free Flight. In 29th AIAA Applied Aerodynamics Conference; 27 30 June 2011; Honolulu, Hawaii; AIAA 2011-3668.
- 12. Konishi Y, Okuizumi H, Ohno T. PIV Measurement of a Flying Table Tennis Ball. In 11th conference of the International Sports Engineering Association, ISEA 2016; 11-14 June 2016; Delft, Netherlands.
- 13. Mehta R. Aerodynamics of sports balls. Ann. Rev. Fluid Mech. 1985; 17: p. 151-189.
- 14. Potts J, Crowther J. Frisbee Aerodynamics. In 20th AIAA Applied Aerodynamics Conference; 24-26 June 2002,; St. Louis, Missouri, USA, AIAA 2002 3150.
- 15. McCoy R. Aerodynamic and flight dynamic characteristics of the new family of 5.56 mm NATO ammunition. BRL memorandum BRL-MR-3476, USA.; October 1985.
- McCoy R. Aerodynamic characteristics of calibre.22 long rifle match ammunition. BRL memorandum BRL-MR-3877, USA.; November 1990.
- 17. McCoy R. The aerodynamic characteristics of 7.62 mm match bullets. BRL memorandum BRL-

- MR-3733, USA.; December 1988.
- 18. Hoerner S. Fluid-dynamic drag: practical information on aerodynamic drag and hydrodynamic resistance USA: Published by the Author; 1965.
- 19. Bailey A, Hiatt J. Free-flight measurements of sphere drag at subsonic, transonic, supersonic, and hypersonic speeds for continuum and near free molecular flow conditions. Report for Office of Aerospace Research, Tech. Rep. AEDC-TR-70-291, USA.; 1971.
- 20. Mair W. Reduction of base drag by boat-tailed afterbodies in low speed flow. Aeronautical Quarterly. 1969; 20: p. 307-320.
- 21. ESDU. Subsonic base drag of cylindrical bodies with conical boat-tails. ESDU, Item 76033, UK.; 1976.
- 22. Viswanath P. Flow management techniques for base and afterbody drag reduction. Prog. Aerospace Science. 1996; 32: p. 79-129.
- 23. Norman A, McKeon B. Effect of sting size on the wake of a sphere at subcritical Reynolds numbers. In 38th Fluid Dynamics Conference; 23-26 June 2008; Seattle, USA; AIAA 2008-4183.
- 24. Hoerner S. Tests of spheres with reference to Reynolds number, turbulence, and surface roughness. NACA Technical Memorandum No. 777. Langley, Virginia:; 1935.
- 25. Bell J, Mehta R. Contraction design for small low-speed wind tunnels. NASA Technical Report CR-182947 (JIAA TR- 84). USA:; April 1988.
- 26. Kitta S, Hasegawa S, Murakami M, al e. Aerodynamic properties of a shuttlecock with spin at high Reynolds number. In 5th Asia-Pacific Congress on Sports Technology (APCST); 28-31 August 2011; Melbourne, Australia.
- 27. Buckholz R. Measurements of unsteady periodic forces generated by the blowfly flying in a wind tunnel. J. Exper. Biol. 1981; 90: p. 63-173.
- 28. Achenbach E. Experiments on the flow past spheres at very high Reynolds numbers. J. Fluid Mech. 1972; 54: p. 565-575.
- 29. Lajos T. Drag reduction by the production of a separation bubble on the front of a bluff body. J. Wind Eng. Ind. Aerodyn. 1986; 22: p. 331-338.
- 30. Son K, Choi J, Jeon W, al e. Effect of free-stream turbulence on the flow over a sphere. Phys. Fluids. 2010; 22: p. 1-7.
- 31. Neve R. The importance of turbulence macroscale in determining the drag coefficient of spheres. Int. J. Heat & Fluid Flow. 1986; 7: p. 28-36.
- 32. Maskell E. A theory of the blockage effects on bluff bodies and stalled wings in a closed wind

- tunnel. ARC Reports and Memoranda (R & M) No. 3400, UK.; Nov. 1963.
- 33. Barlow J, Rae A, Pope W. Low Speed Wind Tunnel Testing. 3rd ed. New York: John Wiley & Sons; 1999.
- 34. Itsweire E, Helland K. A high-performance low-cost constant temperature hot wire anemometer.

 J. Phys. E: Sci. Instrum. 1983; 16: p. 549-553.
- 35. Osorio O, Silin N, Converti J. Fabrication of hot-wire probes and electronics for constant temperature anemometers. Latin Amer. Applied Res. 2010; 40: p. 233-239.
- 36. Bruun H. Hot-wire Anemometry Oxford: Oxford University Press (OUP); 1995.
- 37. Benjamin S, Roberts C. Measuring flow velocity at elevated temperature with a hot wire anemometer calibrated in cold flow. Int. J. Heat and Mass Transf. 2002; 45: p. 703-706.
- 38. Pereira J. Hover and wind-tunnel testing of shrouded rotors for improved micro-air vehicle design. PhD thesis. USA: University of Maryland; 2008.
- 39. Winkler J, Temel F, Carolus T. Concept, design and characterization of a Small aeroacoustic wind tunnel facility with application to fan blade measurements. In Conference Fan Noise; 17-19 September 2007; Lyon, France.
- 40. Nguyen Q. Designing, constructing, and testing a low–speed open–jet wind tunnel. Int. J. Eng. Res. and Appl. 2014; 4: p. 243-246.
- 41. Wolf C. The subsonic near-wake of bluff bodies. PhD thesis. Germany: RWTH Aachen University; 2013.
- 42. Barford N. Experimental measurements: precision, error and truth. 2nd ed. London: John Wiley & Sons; 1985.
- 43. Jourdan G, Houas L, Igra O, al e. Drag coefficient of a sphere in a non-stationary flow: new results. Proc. R. Soc. A. 2007; 463: p. 3323–3345.
- 44. Houghton E, Carpenter P, Collicott S. Aerodynamics for engineering students. 6th ed. Amsterdam: Butterworth-Heinemann (Elsevier); 2012.
- 45. Anderson J. Fundamentals of aerodynamics. 2nd ed. New York: McGraw-Hill; 1991.
- 46. Sadeh W, Saharon D. Turbulence effect on crossflow around a circular cylinder at subcritical Reynolds numbers. NASA Contractor Report 3622. USA:; November 1982.